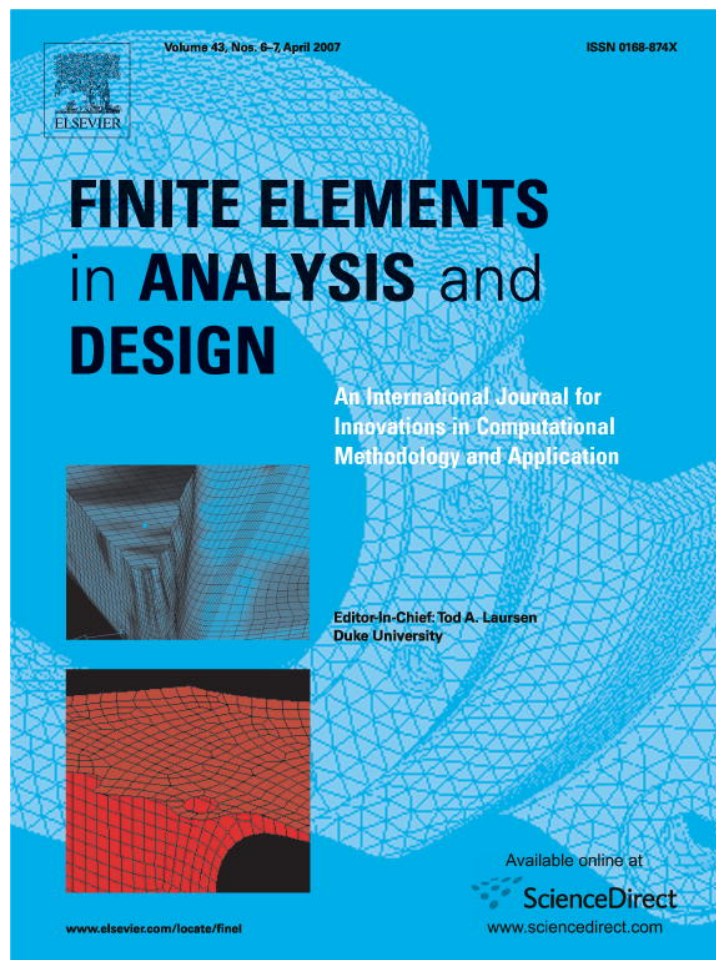


Provided for non-commercial research and educational use only.  
Not for reproduction or distribution or commercial use.



This article was originally published in a journal published by Elsevier, and the attached copy is provided by Elsevier for the author's benefit and for the benefit of the author's institution, for non-commercial research and educational use including without limitation use in instruction at your institution, sending it to specific colleagues that you know, and providing a copy to your institution's administrator.

All other uses, reproduction and distribution, including without limitation commercial reprints, selling or licensing copies or access, or posting on open internet sites, your personal or institution's website or repository, are prohibited. For exceptions, permission may be sought for such use through Elsevier's permissions site at:

<http://www.elsevier.com/locate/permissionusematerial>

# Numerical conformal mapping method based Voronoi cell finite element model for analyzing microstructures with irregular heterogeneities

Abhijeet Tiwary, Chao Hu, Somnath Ghosh\*

Department of Mechanical Engineering, The Ohio State University, 650 Ackerman Road, Columbus, OH 43202, USA

Received 31 July 2006; accepted 2 December 2006  
Available online 26 January 2007

## Abstract

Numerical conformal mapping (NCM) is an effective method for transforming arbitrary polygonal domains into a regular domain such as a unit circle. This paper incorporates NCM-based stress functions in the Voronoi cell finite element model (VCFEM) for modeling microstructures with irregular shaped heterogeneities. Additional stress function components using the multi-resolution wavelet bases are also introduced to enrich stress functions in regions of sharp corners. The resulting enhanced model, termed as NCM–VCFEM, is able to effectively analyze real micrographs of heterogeneous materials with irregular shapes that have considerable effects on the evolution of stresses, strains and local damage. To optimize the use of the expensive NCM–VCFEM elements for the entire microstructure, a method of identification of heterogeneities that cannot be approximated as ellipses is first developed. Subsequently, a tessellation process is devised to accommodate arbitrary shapes in the VCFEM mesh. Validation studies comparing the results of NCM–VCFEM simulations with other numerical and analytical results demonstrate the effectiveness of NCM–VCFEM.

© 2007 Elsevier B.V. All rights reserved.

**Keywords:** Numerical conformal mapping; Voronoi cell finite element model; Multi-resolution wavelets

## 1. Introduction

Mechanical properties of heterogeneous materials, widely used in automotive, aerospace and other engineering systems, depend on morphological characteristics like size, shape and spatial distribution of heterogeneities. The Voronoi cell finite element model (VCFEM), developed by Ghosh et al. [1–7] has been very effective in modeling heterogeneous microstructures of composite and porous materials with heterogeneities (fibers, particles or voids) of regular shapes like circles and ellipses. While the name Voronoi cell has been historically used because of its association with point seeds in the tessellation process, the cells used in VCFEM are in general arbitrary and do not conform to the strict definitions of Voronoi cells. In VCFEM, each cell with embedded heterogeneities represents the neighborhood or regions of influence for the heterogeneity. Each cell consisting of a heterogeneity and its neighborhood surrounding matrix, as shown in Fig. 1c, is treated as a single

super-element and requires no further subdivision for variable interpolation further subdivision. VCFEM incorporates an assumed stress hybrid formulation. Independent assumptions are made for equilibrated stress field in the interior of each element including the matrix and inclusion phases. Furthermore, compatible displacement fields are assumed on the cell element boundary as well as on the matrix-inclusion interface. Incorporation of known functional forms for regular heterogeneities from analytical micromechanics makes this element very effective for micromechanical analyses and substantially enhances its convergence.

Heterogeneities in real materials often have very irregular shapes as seen in the micrograph of a cast Aluminum alloy in Fig. 1(a). Shen et al. [8] have evaluated the effective elastic response of composites with polygonal inclusions. The classical Eshelby's inclusion problem for polygons and polyhedra have been solved by Rodin [9] and Kawashita and Nozaki [10] for an infinite elastic body. Analysis methods for polygonal heterogeneities with built-in singularities at the sharp corners have been developed in [9,11]. Tsukrov and Novak [12] have developed a finite element analysis method using numerical

\* Corresponding author. Tel.: +1 614 292 2599; fax: +1 614 292 7369.  
E-mail address: [ghosh.5@osu.edu](mailto:ghosh.5@osu.edu) (S. Ghosh).

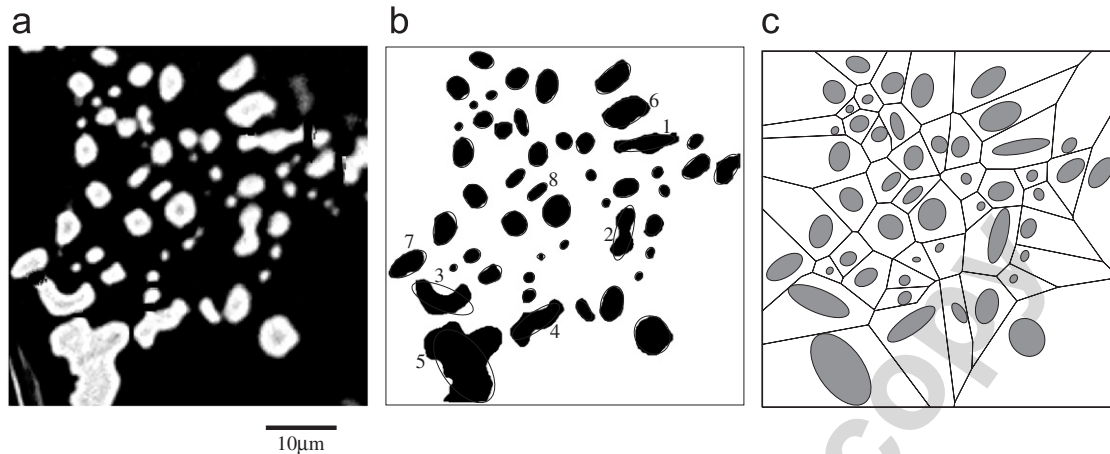


Fig. 1. (a) SEM micrograph of a cast aluminum alloy Al319 microstructure with irregular silicon particulates, (b) a filtered black and white image micrograph with superposed equivalent elliptical contours and (c) the equivalent microstructure of elliptical particles meshed using modified Voronoi tessellation.

conformal mapping (NCM) to calculate effective elastic properties of materials with irregular shaped heterogeneities. The method is very effective for predicting the macroscopic properties of material but it does not deal with local stress concentrations. Ishikawa and Kohno [11] have used conformal mapping and the Goursat stress functions to analyze the stress singularity at the corner of rigid square inclusion in the infinite plate. In this paper, an NCM-based Voronoi cell FEM or NCM–VCFEM is developed for analysis and local stress distributions in microstructures having arbitrary shaped heterogeneities. Shape-based stress functions are developed in NCM–VCFEM using the Schwarz–Christoffel transformations [13,14] for mapping arbitrary polygons to a unit circle. The resulting stress functions conform to the shape of the interface in its vicinity and decays rapidly with distance away from the interface. Very high stress gradients develop in the vicinity of sharp corners in the interface. Even at distances away from the interface, the quality of solution is affected by the choice of the stress functions. Wavelet basis functions [15,16] are very effective for problem with high solution gradients and have been used in [7] to model moving singularities with evolving cracks. Multi-resolution wavelet bases are consequently used to enrich stress representations in the neighborhood of the corners and capture the steep stress gradients.

This paper starts with a brief introduction of microstructure simulation for optimal representation, followed by tessellation for generating the NCM–VCFEM mesh. The VCFEM formulation with NCM implementation is then discussed for heterogeneities of arbitrary shapes. Numerical examples are finally conducted to validate the accuracy of NCM–VCFEM in comparison with analytical and numerical solutions using commercial codes.

## 2. The VCFEM preprocessor for microstructures containing irregular shaped heterogeneities

Dirichlet tessellation of a planar domain is defined as the subdivision of a plane containing a dispersed set of

points such that each point has associated with it a region of plane that is closest to it than to any other [17,18]. Let  $P = \{p_1, \dots, p_i, \dots, p_n; 2 \leq n < \infty\}$  represent a set of  $n$  independent points or seeds, dispersed in plane with coordinates  $x_i \neq x_j \in \mathcal{R}^2, \forall i \neq j; i, j \in I_n$ . The region defined as

$$V_i = \{x : \|x - x_i\| \leq \|x - x_j\| \forall j \neq i, j \in I_n\} \quad (1)$$

represents a Voronoi polygon associated with the point generator  $p_i \in \mathcal{R}^2$ . The Voronoi polygon  $V(p_i)$  encompasses all points whose distances to  $p_i$  are less than the distance to any other point  $p_j$  in the 2D space. Each polygon is the intersection of open half planes bounded by perpendicular bisectors of lines joining a generator  $p_i$  with each of its neighbors  $p_j$ . The boundary segment  $B_{ij}$ , common to polygons  $V_i$  and  $V_j$ , are nearer to the points  $p_i$  and  $p_j$  than to any other labeled point in the domain and is denoted as

$$B_{ij} = \{x : \|x - x_i\| = \|x - x_j\| \leq \|x - x_k\| \forall k \neq i, j\}. \quad (2)$$

Subsequently, the vertex  $v_{ijk}$  common to polygons  $V_i, V_j$  and  $V_k$  is equidistant from three or more generating points  $p_i, p_j$  and  $p_k$

$$v_{ijk} = \{x : \|x - x_i\| = \|x - x_j\| = \|x - x_k\| \leq \|x - x_l\| \forall l \neq i, j, k\}. \quad (3)$$

The aggregate of all polygons, represented by the set  $\mathcal{V} = \{V_1, \dots, V_n\}$  represents a Voronoi mesh generated for the point set  $P$ . For real materials like composites, porous materials or alloys with precipitates and inclusions, the heterogeneities can rarely be approximated as points. A micrograph of a cast aluminum alloy Al-319 consisting of intermetallics and Si particulates is shown in Fig. 1a. Fig. 1b is a black and white image of the microstructure obtained after filtering out noise in the micrograph using thresholding techniques [19]. Accurate representation of the shape and size of heterogeneities is needed to model these microstructures for material properties. Equivalent microstructures, with heterogeneities of arbitrary shapes approximated as ellipses (in 2D) or ellipsoids (in 3D), have

been generated in [20–22]. In this process, the zeroth order moment ( $I_0$ ), the first order moments ( $I_x, I_y$ ), and the second order moments ( $I_{xx}, I_{yy}, I_{xy}$ ) of the digitized heterogeneity in the micrographs are equated with those for the equivalent ellipses or ellipsoids. In 2D, the moments of the digitized heterogeneity (dh) are computed as the sum of moments of all pixels contained within its boundary, i.e.

$$\begin{aligned} \text{dh} I_0 &= \sum_{I=1}^{\# \text{ of pixels}} A_I \quad (\text{a}), \\ \text{dh} I_x &= \sum_{I=1}^{\# \text{ of pixels}} x_I A_I, \quad \text{dh} I_y = \sum_{I=1}^{\# \text{ of pixels}} y_I A_I \quad (\text{b}), \\ \text{dh} I_{xx} &= \sum_{I=1}^{\# \text{ of pixels}} y_I^2 A_I, \quad \text{dh} I_{yy} = \sum_{I=1}^{\# \text{ of pixels}} x_I^2 A_I, \\ \text{dh} I_{xy} &= \sum_{I=1}^{\# \text{ of pixels}} x_I y_I A_I \quad (\text{c}), \end{aligned} \quad (4)$$

where  $x_I, y_I, A_I$  correspond to the centroidal coordinates and area of the  $I$ th pixel in the image. The procedure yields the centroid ( $x_c, y_c$ ), the major and minor axes ( $a, b$ ), and angular orientation  $\theta$  of the major axis of the equivalent ellipse in the following sequence:

- First, the centroidal coordinates are evaluated using equations

$$x_c = \frac{\text{dh} I_x}{\text{dh} I_0}; \quad y_c = \frac{\text{dh} I_y}{\text{dh} I_0}. \quad (5)$$

- Next, the second moments are written in terms coordinates with origin at  $x_c, y_c$  as  $\text{dh} I_{xy}^c, \text{dh} I_{yy}^c, \text{dh} I_{xx}^c$ . The ellipse orientation  $\theta$  corresponds to that for which the rotated  $\text{dh} I_{xy}^{c'} = 0$ , where the superscript  $c'$  corresponds to a centroidal coordinate system that is oriented along the principal axes of the ellipse. The major axis orientation is given as

$$\theta = \frac{1}{2} \tan^{-1} \left( \frac{-2 \text{dh} I_{xy}^c}{\text{dh} I_{xx}^c - \text{dh} I_{yy}^c} \right). \quad (6)$$

- Finally, the lengths of the major and minor axes ( $a$  and  $b$ ) are calculated from moments in the rotated coordinate system as

$$b = \left( \frac{4 \text{dh} I_{xx}^{c'}}{\text{dh} I_0} \right)^{1/2} \quad \text{and} \quad a = \frac{\text{dh} I_0}{\pi b}. \quad (7)$$

Fig. 1b shows the contours of the resulting ellipses in the equivalent microstructure, constructed by this process, overlapped by the real contours. While the difference between the real and equivalent boundary contours may not be appreciable for many inclusions, it can be large for a few inclusions.

Voronoi tessellation methods have been augmented in [6,22,23] to accommodate elliptical or ellipsoidal shapes of different sizes. Interference with heterogeneities of finite size is avoided by surface-based tessellation algorithms followed

Table 1

Error measures used in the criteria for determining non-elliptical inclusions

Inclusion No.	$e_{I_{yy}}(\%)$	Irregularity factor ( $IF$ ) = $\chi \cdot \rho$
1	15.6	0.151
2	24.5	0.229
3	36.3	0.271
4	22.2	0.206
5	26.8	0.254
6	4.8	0.357
7	3.4	0.356
8	3.3	0.327

by minor edge re-orientation. A tessellated domain for the equivalent microregion of Fig. 1b with 49 elliptical inclusions is shown in Fig. 1c. It is advantageous to represent inclusions by elliptical shapes for inclusions from a modeling point of view. Significant computational efficiency can be achieved in the Voronoi cell finite element modeling when the interface is represented as an ellipse due to their well known properties and micromechanics results, as discussed in [1,2]. However, when the shapes differ significantly, e.g. inclusions 2, 3, and 5 in Fig. 1b, elliptical representation will lead to erroneous predictions in local stresses and strains. Hence, it is necessary to retain their complex shape without simplifications, even though the associated cost of analysis is considerably higher than their elliptical counterparts. Thus, the minimum number of inclusions that cannot be approximated as ellipses is decided prior to tessellation to facilitate efficient VCFEM-based simulation. Two criteria are set to distinguish between heterogeneities that can be approximated as ellipses from those that cannot. The first criterion is based on the error in the second order moment  $I_{yy}$  that is not used in the parameter evaluation of Eqs. (6) and (7).

$$e_{I_{yy}}(\%) = \frac{(\text{dh} I_{yy} - \text{ellipse } I_{yy})}{\text{dh} I_{yy}} * 100. \quad (8)$$

The error  $e_{I_{yy}}$  for different inclusions in Fig. 1b are tabulated in Table 1.  $e_{I_{yy}}$  is large for inclusions that are visually not close to the elliptical shape. A second shape-based criterion, involving roundness ( $\rho$ ) and edge smoothness ( $\chi$ ) of the image [19,24] is also used. Roundness ( $\rho = 4A/\pi d_{\max}^2$ ) is a measure of how close the heterogeneity is to a circle. It is effective for heterogeneities of arbitrary shape for which the aspect ratio is not well defined.  $\rho^i$  varies from 1 for circular shapes to 0 for highly elongated phases. The edge smoothness ( $\chi = \sqrt{4\pi^2 A d_{\max}/P^3}$ ), is a measure of surface irregularities, e.g. sharp corners, even if it has an overall high roundness. Here  $A$  is the area,  $d_{\max}$  is the farthest distance between two points on the boundary and  $P$  is the perimeter.  $\chi$  closer to 0 indicates a large number of surface irregularities. Using the above shape parameters, a criterion is defined for a heterogeneity to be represented as an ellipse as

$$\text{Irregularity factor } (IF) = \rho * \chi \leq \text{specified tolerance}. \quad (9)$$

$IF$  varies between 0.0 and 1.0. The product compounds the effect of the individual parameters to signal departure from smooth low aspect ratio elliptical shapes. In this study, the tolerance is taken as 0.3. The values of  $IF$  for the 8 inclusions

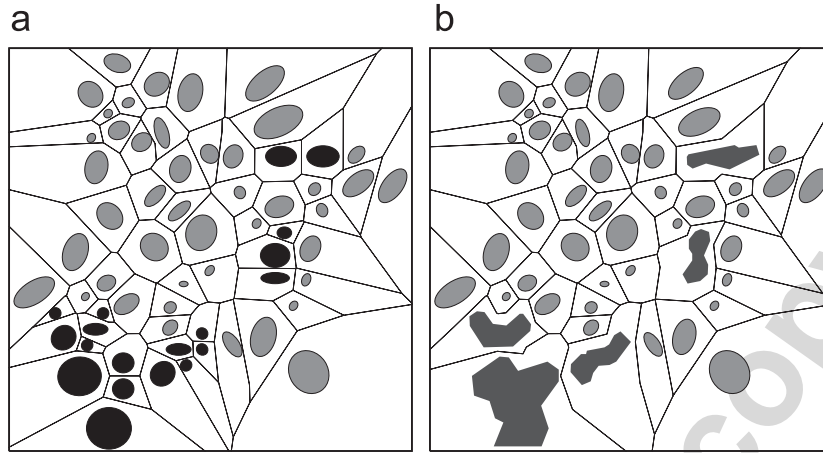


Fig. 2. A VCFEM mesh by modified Voronoi tessellation for the simulated micrograph with (a) all particles simulated as ellipses and (b) minimum number of particles of arbitrary shapes and the rest ellipses.

are again calculated in Table 1. Both of these criteria in Eqs. (8) and (9) infer that the inclusions 1–5 cannot be approximated as ellipses.

### 2.1. Modified tessellation for heterogeneities of irregular shapes

Modifications in the tessellation algorithms for elliptical inclusions in [6,22,23] are needed for heterogeneities of irregular shapes. This is based on a divide and conquer algorithm, as described below:

1. Inclusions of irregular shape are represented as multi-sided polygons. Polygonal inclusions are constructed with the lowest possible number of sides for which the difference in area from the parent digital image, obtained by adding included pixel areas, is a minimum.
2. Each polygon is encased in the smallest possible square, which is discretized into a  $n * n$  uniform square grid. The number  $n$  is chosen such that the size of each subgrid square is smaller than the smallest polygon edge.
3. Core regions of square elements belonging to each polygon are retained by eliminating all the subgrid squares that are external to the area enclosed by each polygon. Intersection of each subgrid with the polygon edges is checked for retention. The core subregion for each polygon is further divided into non-intersecting rectangles of the biggest possible size.
4. Each rectangle is inscribed within the largest possible ellipse. This intermediate microstructure containing only elliptical shape inclusions (see Fig. 2a) is tessellated by the mesh generator for elliptical particles that is developed in [6,22,23].
5. The tessellated Voronoi polygons surrounding the component ellipses are merged to generate the final Voronoi polygon for each irregular shaped heterogeneity as shown in Fig. 2b.

This microstructure with tessellation constitutes the input mesh for the VCFEM.

### 3. NCM-VCFEM for micromechanics of irregular heterogeneities

VCFEMs have been developed for a wide variety of micromechanics problems in [1–3,7]. Only the essential formulation is summarized here for completeness in the context of discussing the NCM implementation for heterogeneities of irregular shapes. The assumed stress hybrid formulation in VCFEM allows independent interpolations of equilibrated stress fields  $\sigma_{ij}^m$  in the matrix phase  $\Omega_m$  and  $\sigma_{ij}^c$  in the inclusion phase  $\Omega_c$  of each Voronoi cell element  $\Omega_e$ . Stress interpolations in each phase are expressed as

$$\{\sigma^m\} = [\mathbf{P}^m]\{\beta^m\} \text{ in } \Omega_m \quad \text{and} \quad \{\sigma^c\} = [\mathbf{P}^c]\{\beta^c\} \text{ in } \Omega_c. \quad (10)$$

The matrices  $[\mathbf{P}^m]$  and  $[\mathbf{P}^c]$  in 2D may be obtained from equilibrated stress functions like the Airy's stress function, and  $\{\beta^m\}$  and  $\{\beta^c\}$  are unknown coefficients to be solved. In addition, independent compatible displacement fields  $u_i^e$  and  $u_i^c$  are assumed on each Voronoi cell element boundary  $\partial\Omega_e$  and on the matrix-inclusion interface  $\partial\Omega_c$ , respectively, and are interpolated as

$$\{u^e\} = [\mathbf{L}^e]\{q^e\} \text{ on } \partial\Omega_e \quad \text{and} \quad \{u^c\} = [\mathbf{L}^c]\{q^c\} \text{ on } \partial\Omega_c. \quad (11)$$

The complimentary energy functional for each element is expressed in terms of the internal stresses and boundary displacements as

$$\begin{aligned} \Pi_e(\sigma_{ij}^m, \sigma_{ij}^c, u_i^e, u_i^c) = & - \int_{\Omega_m} B^m(\sigma_{ij}^m) d\Omega - \int_{\Omega_c} B^c(\sigma_{ij}^c) d\Omega \\ & + \int_{\partial\Omega_e} \sigma_{ij}^m n_j^e u_i^e d\partial\Omega - \int_{\Gamma_{te}} \bar{t}_i u_i^e d\Gamma \\ & - \int_{\partial\Omega^c} (\sigma_{ij}^m - \sigma_{ij}^c) n_j^c u_i^c d\partial\Omega. \end{aligned} \quad (12)$$

For linear elasticity,  $B = \frac{1}{2} S_{ijkl} \sigma_{ij} \sigma_{kl}$  is the complementary energy density with  $S_{ijkl}$  the compliance tensor, and  $\bar{t}_i$  is the prescribed traction on the boundary  $\Gamma_{te}$ . Vectors  $\mathbf{n}^e$  and  $\mathbf{n}^c$  are

the outward normal on  $\partial\Omega_e$  and  $\partial\Omega_c$ , respectively. The total potential energy functional for all elements in the ensemble, containing  $N$  Voronoi cell elements is expressed as

$$\Pi = \sum_{e=1}^N \Pi_e. \quad (13)$$

Substituting the stress interpolations in (10) and the displacement interpolations (11) in Eq. (12), and setting the variations with respect to the stress coefficients  $\beta^m$  and  $\beta^c$ , respectively, to zero, results in the weak form of the element kinematic relation:

$$\begin{aligned} & \left[ \int_{\Omega_m} [\mathbf{P}^m]^T [\mathbf{S}^m] [\mathbf{P}^m] d\Omega \quad \mathbf{0} \right. \\ & \quad \left. \mathbf{0} \quad \int_{\Omega_c} [\mathbf{P}^c]^T [\mathbf{S}^c] [\mathbf{P}^c] d\Omega \right] \begin{Bmatrix} \beta^m \\ \beta^c \end{Bmatrix} \\ & = \left[ \int_{\partial\Omega_e} [\mathbf{P}^m]^T [\mathbf{n}^e] [\mathbf{L}^e] d\partial\Omega \quad - \int_{\partial\Omega_c} [\mathbf{P}^m]^T [\mathbf{n}^c] [\mathbf{L}^c] d\partial\Omega \right. \\ & \quad \left. \mathbf{0} \quad \int_{\partial\Omega_c} [\mathbf{P}^c]^T [\mathbf{n}^c] [\mathbf{L}^c] d\partial\Omega \right] \\ & \quad \times \begin{Bmatrix} \mathbf{q}^e \\ \mathbf{q}^c \end{Bmatrix}. \end{aligned}$$

The kinematic Eq. (14) can be expressed in a condensed form as the matrix equation

$$\begin{bmatrix} \mathbf{H}_m & \mathbf{0} \\ \mathbf{0} & \mathbf{H}_c \end{bmatrix} \begin{Bmatrix} \beta^m \\ \beta^c \end{Bmatrix} = \begin{bmatrix} \mathbf{G}_e & -\mathbf{G}_{mc} \\ \mathbf{0} & \mathbf{G}_{cc} \end{bmatrix} \begin{Bmatrix} \mathbf{q}_e^E \\ \mathbf{q}_e^c \end{Bmatrix} \quad \forall e = 1, \dots, N. \quad (14)$$

Subsequently, setting the first variation of the total energy functional  $\Pi$  in Eq. (13) with respect to  $\{\mathbf{q}^e\}$  and  $\{\mathbf{q}^c\}$  to zero, results in the weak form of the traction reciprocity conditions:

$$\begin{aligned} & \sum_{e=1}^N \left[ \int_{\partial\Omega_e} [\mathbf{L}^e]^T [\mathbf{n}^e]^T [\mathbf{P}^m] d\Omega \quad \mathbf{0} \right. \\ & \quad \left. - \int_{\partial\Omega_c} [\mathbf{L}^c]^T [\mathbf{n}^c]^T [\mathbf{P}^m] d\Omega \quad \int_{\partial\Omega_c} [\mathbf{L}^c]^T [\mathbf{n}^c]^T [\mathbf{P}^c] d\Omega \right] \\ & \quad \times \begin{Bmatrix} \beta^m \\ \beta^c \end{Bmatrix} = \sum_{e=1}^N \left\{ \int_{\Gamma_t} [\mathbf{L}^e]^T \{\bar{\mathbf{t}}\} d\Omega \right. \\ & \quad \left. \mathbf{0} \right\}. \end{aligned} \quad (15)$$

Substituting Eq. (14) in the global traction reciprocity Eq. (15) yields the matrix equation:

$$\begin{aligned} & \sum_{e=1}^N \begin{bmatrix} \mathbf{G}_e & -\mathbf{G}_{mc} \\ \mathbf{0} & \mathbf{G}_{cc} \end{bmatrix}^T \begin{bmatrix} \mathbf{H}_m & \mathbf{0} \\ \mathbf{0} & \mathbf{H}_c \end{bmatrix} \begin{bmatrix} \mathbf{G}_e & -\mathbf{G}_{mc} \\ \mathbf{0} & \mathbf{G}_{cc} \end{bmatrix} \begin{Bmatrix} \mathbf{q}^e \\ \mathbf{q}^c \end{Bmatrix} \\ & = \sum_{e=1}^N \left\{ \int_{\Gamma_t} [\mathbf{L}^m]^T \{\bar{\mathbf{t}}\} d\Omega \right. \\ & \quad \left. \mathbf{0} \right\}. \end{aligned} \quad (16)$$

With known tractions and displacements on  $\Gamma_t$  and  $\Gamma_u$ , respectively, the global traction reciprocity condition (16) is solved for the generalized displacements.

### 3.1. Special stress functions accounting for shape of heterogeneities

An important criterion affecting the convergence of the multi-phase Voronoi cell elements is the optimal representation of stress fields in each constituent phase. Equilibrated stresses in VCFEM are obtained from the second derivatives of stress functions (e.g. Airy's function in 2D) with respect to  $x$  and  $y$

coordinates. It has been observed in [1] that even very high order polynomials in a pure polynomial representation of stress functions are not able to efficiently account for the shape of the matrix-inclusion interface, resulting in poor convergence characteristics. In [1–3], special matrix stress functions have been developed from analogous micromechanics solutions to enhance element efficiency and convergence properties. Conditions that govern the choice of these stress functions are:

1. For matrix stress functions, shape effects should be strong near the interface and recede with increasing distances from it.
2. Consideration of shape effects in matrix stress functions should facilitate traction reciprocity at the matrix-inclusion interface.

Consequently, the matrix stress function in [1–3] is decomposed into two parts, i.e.  $\Phi^m = \Phi_{\text{poly}}^m + \Phi_{\text{rec}}^m$ . The pure polynomial function  $\Phi_{\text{poly}}^m$  accommodates the far field stress in the matrix. The reciprocal function  $\Phi_{\text{rec}}^m$  follow from the analytical stress solutions derived by Muskhelishvili [25]. It facilitates interfacial stress concentration, while accounting for its shape, and decays with increasing distance from the interface. Inclusion stress functions are interpolated using pure polynomial functions, i.e.  $\Phi_{\text{poly}}^c$ . The polynomial stress functions are written in terms of scaled local coordinates  $(\xi, \eta)$  with origin at the element centroid  $(x_c, y_c)$ , as

$$\Phi_{\text{poly}}^m = \sum_{p,q} \xi^p \eta^q \beta_{pq}^m \quad \text{and} \quad \Phi_{\text{poly}}^c = \sum_{p,q} \xi^p \eta^q \beta_{pq}^c, \quad (17)$$

where

$$\xi = (x - x_c)/L_e, \quad \eta = (y - y_c)/L_e \quad (18)$$

and the scaling parameter for each element is  $L_e = \sqrt{\max(x - x_c) \times \max(y - y_c)} \forall (x, y) \in \partial\Omega_e$ . The use of the local coordinates  $(\xi, \eta)$  instead of global coordinates  $(x, y)$  prevents ill conditioning of the stiffness matrix due to high exponents of  $(x, y)$  in  $\Phi^m$  and  $\Phi^c$ . The reciprocal stress function  $\Phi_{\text{rec}}^m$  is expressed as

$$\begin{aligned} \Phi_{\text{rec}}^m & = \sum_{p,q} \xi^p \eta^q \sum_{i=1}^n \frac{1}{\hat{f}_{p+q+i-1}} \beta_{pqi}^m \\ & = \sum_{p,q} \xi^p \eta^q \left( \frac{\beta_{pq1}^m}{\hat{f}_{p+q}} + \frac{\beta_{pq2}^m}{\hat{f}_{p+q+1}} + \dots \right) \end{aligned} \quad (19)$$

in which a radial function  $\hat{f}(x, y)$  is constructed to possess the properties

$$\begin{aligned} \hat{f}(x, y) & = 1 \quad \text{on} \quad \partial\Omega_c^m \quad \text{and} \\ \frac{1}{\hat{f}(x, y)} & \rightarrow 0 \quad \text{as} \quad (x - x_c, y - y_c) \rightarrow \infty. \end{aligned} \quad (20)$$

For elliptical heterogeneities defined by the equation  $x^2/a^2 + y^2/b^2 = 1$ , a conformal mapping function may be used to construct the radial function through a map of the elliptical domain onto a unit circle. Following [25], the function is given

as  $\hat{f} = \sqrt{\psi^2 + \gamma^2}$ , where the transformed coordinates  $(\psi, \gamma)$  are obtained as solutions to the complex quadratic equation:

$$(\psi + i\gamma)^2 - \frac{2(x + iy)(\psi + i\gamma)}{(a + b)} + \frac{(a - b)}{(a + b)} = 0. \quad (21)$$

The analytical conformal mapping function will not hold when heterogeneities discussed in Section 2 cannot be approximated as ellipses. A special method is needed for constructing a mapping function, which maps an arbitrary shape to a circular domain of unit radius.

### 3.2. NCM for constructing the radial functions

NCM using the Schwarz–Christoffel transformation, has been developed by Trefethen and Driscoll [13,14] and has proven to be a very useful method in mapping any arbitrary shape to a unit circle. Square shaped inclusions have been effectively transformed by NCM in [11]. Effective elastic properties of solids with defects and pores of irregular shape have been evaluated using NCM in [12,26]. The present work implements numerical conforming mapping using the Schwarz–Christoffel transformation to generate stress function for heterogeneities with arbitrary shapes. Conformal mapping involves a one-to-one mapping of an open region in the complex plane to another by an analytic function, while preserving angles between intersecting arcs. Schwarz–Christoffel transformation is based on the following postulate:

- Let  $D$  be a simply connected region in a complex polygonal plane bounded by a polygon  $P$  with  $N$  vertices at  $w_1, w_2, \dots, w_N$  having exterior angles  $\pi\beta_k$ , where  $-1 \leq \beta_k \leq 1$ . Then there exists an analytic function  $f(z)$  which maps the unit disk in the complex canonical plane conformally onto  $D$  that can be written as (see [27])

$$w = f(z) = A + C \int_0^z \prod_{k=1}^N \left(1 - \frac{\zeta}{z_k}\right)^{-\beta_k} d\zeta, \quad (22)$$

where  $A$  and  $C$  are complex constants ( $C \neq 0$ ). Here  $z = \psi + iy$  corresponds to a point in the complex canonical plane and  $w = x + iy$  is its corresponding map in the complex polygonal plane. The function  $f(z)$  maps the inside of a polygon to the inside of a unit circle and  $z_1, z_2, \dots, z_N$  are ‘pre-vertices’ on the boundary of the unit circle. However, in VCFEM, the reciprocal function  $\Phi_{\text{rec}}^m$  is needed for the matrix region outside of the polygonal inclusion. Consequently, a modified Schwarz–Christoffel transformation that maps the exterior of a polygon to the interior of a unit circle is utilized as suggested in [14]. The corresponding transformation is

$$w = f(z) = A + C \int_0^z \zeta^{-2} \prod_{k=1}^N \left(1 - \frac{\zeta}{z_k}\right)^{-\beta_k} d\zeta. \quad (23)$$

Fig. 3(a) shows a typical Voronoi cell element containing a polygonal heterogeneity. The forward ( $f(z)$ ) and inverse ( $g(w)$ ) mapping of the matrix region outside of the heterogeneity onto the inside of a unit circle is shown in Figs. 3(b)

and (c). Due to the lack of a continuous functional representation of the heterogeneity boundary, it is not possible to implement this transformation analytically, and hence an NCM is implemented. Developments in this work follow a computationally efficient and accurate algorithm developed in [13,14]. This algorithm, depicted in the flow chart of Fig. 4, consists of three major tasks that are discussed below:

1. *Parameter evaluation:* This task entails evaluation of the mapping parameters  $C$  and  $z_k$ ’s for a polygon  $P$  by solving Eq. (23) with known at  $w_1, w_2, \dots, w_N$ . The set of ‘accessory’ parameters uniquely define the mapping function for  $P$ . In Eq. (23) there are  $N + 2$  unknowns (2 from the real and imaginary parts of  $C$  and  $N$  values of  $z_k$ ). It is important to suppress the rigid body modes of  $P$  by imposing three constraints (in 2D), prior to evaluating these parameters. In the exterior map, two degrees of freedom are naturally constrained, since the center of the unit circle in canonical domain is mapped to infinity in polygonal domain, i.e.  $f(0) = \infty$ . The third degree of freedom is suppressed by imposing an added constraint  $z_N = 1$ . Thus, a total of  $N - 1$  equations should be solved to evaluate the accessory parameters. For a closed polygon, the locations of the pre-vertices ( $z_k$ ) are related to the lengths of the edges of the polygons and their ratios are used in the evaluation. From Eq. (23), the distance between vertices at  $w_j$  and  $w_{j+1}$  is expressed as

$$|w_{j+1} - w_j| = \left| C \int_{z_j}^{z_{j+1}} f'(\zeta) d\zeta \right|. \quad (24)$$

The parameters  $C$  can be eliminated using the ratio of the lengths, resulting in a set of  $(N - 3)$  equations

$$\frac{\left| \int_{z_j}^{z_{j+1}} f'(\zeta) d\zeta \right|}{\left| \int_{z_1}^{z_2} f'(\zeta) d\zeta \right|} = \frac{|w_{j+1} - w_j|}{|w_2 - w_1|}, \quad j = 2, 3, \dots, N - 2. \quad (25)$$

Two more equations are needed to solve for the  $N - 1$  parameters. The analytic or holomorphic mapping function  $f(z)$  requires it to be infinitely differentiable at each point in the domain  $R$  and hence its residue about any point in region  $R$  should be zero. For a given function  $f(z)$  with a pole of order  $m$  at  $z = z_0$ , the residue is expressed as

$$\text{Res}_{(z=z_0)} f(z) = \frac{1}{(m - 1)!} \frac{d^{m-1}}{dz^{m-1}} [(z - z_0)^m f(z)]_{z=z_0}. \quad (26)$$

The analytical expression for  $f'(z)$  in the Schwarz–Christoffel transformation is

$$f'(z) = Cz^{-2} \prod_{k=1}^N \left(1 - \frac{z}{z_k}\right)^{-\beta_k} \quad (27)$$

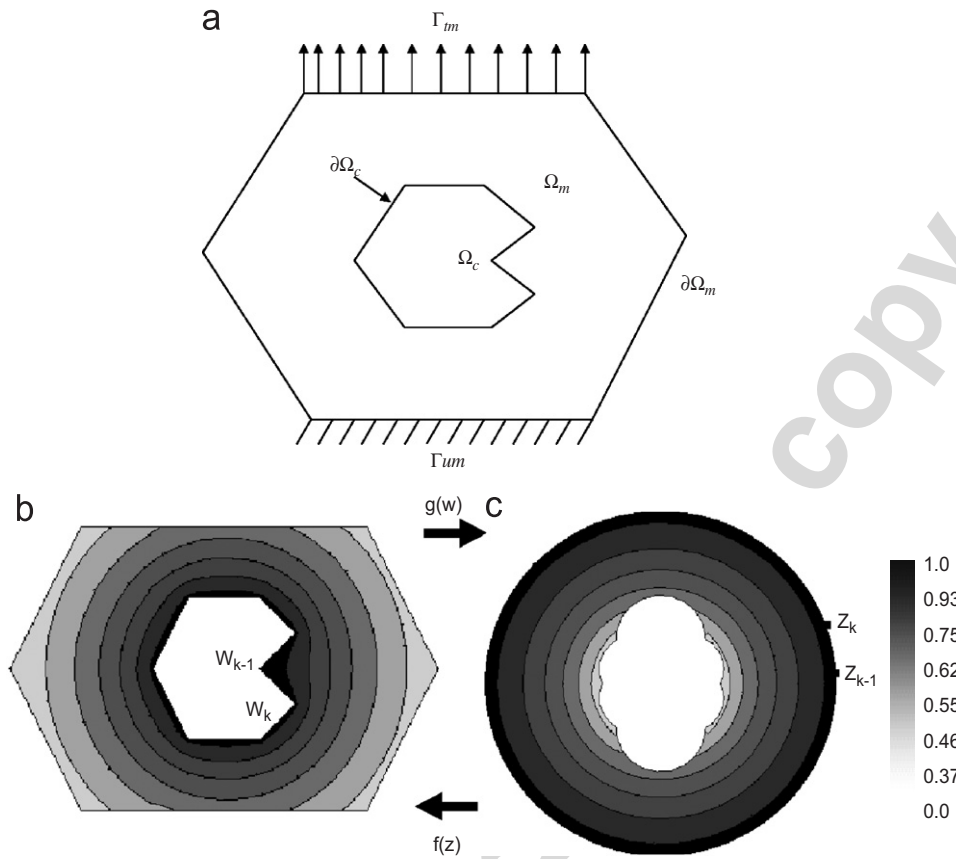


Fig. 3. (a) A basic Voronoi cell element including an irregular polygonal inclusion, (b) contour plot of the inverse mapping function in a complex polygonal plane, and (c) contour plot of the mapping function in a complex canonical plane for numerical conformal mapping (NCM).

which has a pole of order 2 at  $z = 0$ . For this mapping to be analytic, the residue of  $f'(z)$  at  $z = 0$  should be zero. Using Eqs. (26) and (27), this condition becomes

$$\begin{aligned} \text{Res}_{(z=0)} f'(z) &= \frac{d}{dz} \left( C \prod_{k=1}^N \left( 1 - \frac{z}{z_k} \right)^{-\beta_k} \right)_{z=0} \\ &= C \sum_{k=1}^N \frac{\beta_k}{z_k} = 0. \end{aligned} \quad (28)$$

Eqs. (25) and (28) together form a system of  $(N - 1)$  non-linear equations to be solved. An additional constraint needs to be imposed on the vertex coordinates  $z_k = r e^{i\theta} = e^{i\theta}$ , since the radial coordinate  $r = 1$  on the circumference of the unit circle. Starting with a chosen vertex as the reference, i.e.  $\theta_1 = 0$ , the vertices may be arranged in an ascending order of angular coordinates as

$$0 = \theta_1 < \theta_k < \theta_{k+1} < \theta_{N-1} = 2\pi, \quad 1 \leq k \leq N - 1. \quad (29)$$

A simple transformation in terms of a new variable  $\phi_k$  can relax the above constraint to facilitate the

solution process.

$$\phi_k = \log \left( \frac{\theta_k - \theta_{k-1}}{\theta_{k+1} - \theta_k} \right), \quad 1 \leq k \leq N - 1. \quad (30)$$

A quasi-Newton non-linear solver that uses steepest descent search in early iterations is used to solve for the mapping parameters [13].

2. *Forward mapping:* This mapping  $w = f(z)$  in Eq. (23) from the unit circle to the outside of the polygon, determines the image  $w = x + iy$  in polygonal plane for a given point  $z = \psi + i\gamma$  in complex canonical plane. The integral in Eq. (23) may be evaluated over a line joining one of the pre-vertices  $z_k$  to any point  $z$  in the canonical plane. A linear integration path can be chosen, because any line joining a boundary point to interior point of the circle will be entirely contained in it.
3. *Inverse mapping:* An inverse mapping  $z = g(w)$  is invoked to find the image  $z = \psi + i\gamma$  in complex canonical plane for a given point  $w = x + iy$  in polygonal plane, as shown in Figs. 3(b) and (c). Evaluation of the inverse map is more involved than the forward map. This requires the evaluation of  $z = g(w)$  for given values of  $w$ . As the form of function  $g(w)$  is not known a priori, a non-linear equation  $w = f(z)$  needs to be solved to find the inverse

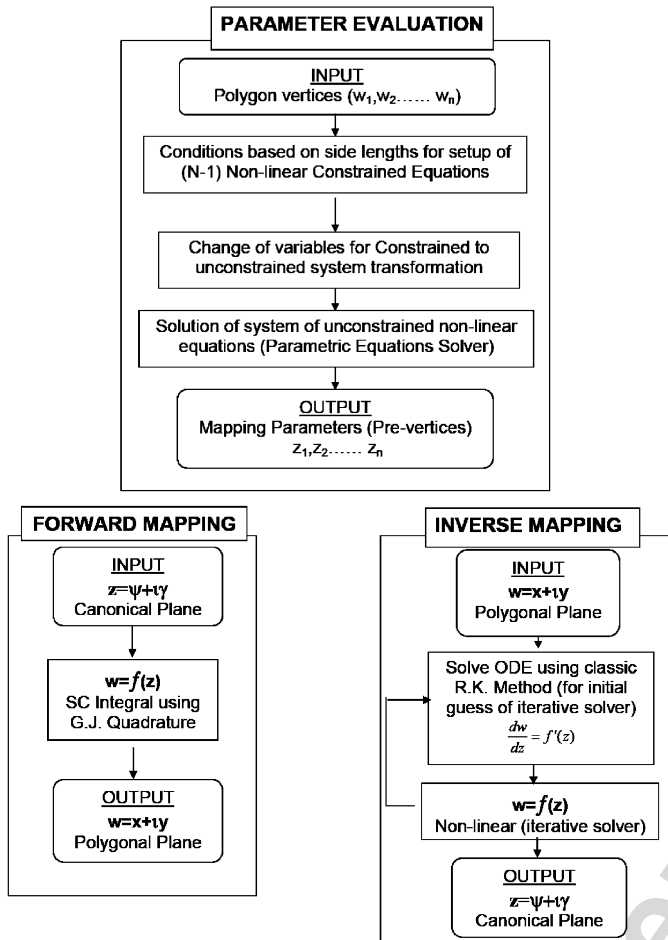


Fig. 4. Flow chart of operations in the numerical conformal mapping (NCM) routine in VCFEM.

map. This is accomplished in a two step process. Taking the derivative of Eq. (23) with respect to  $w$ , yields

$$\frac{dz}{dw} = \frac{1}{C} \prod_{k=1}^N \left(1 - \frac{z}{z_k}\right)^{\beta_k} \quad (31)$$

If a vertex and its map  $(z_0, w_0)$  are known, then  $z=g(w)$  at any other point can be computed by numerically solving this ordinary differential equation. For computational efficiency, the pair  $(z_0, w_0)$  is chosen from a set of points on the boundary such that  $|w - w_0|$  is a minimum. The above differential equation is then solved by the Runge–Kutta method with  $(z_0, w_0)$  as the initial conditions. The resulting solution obtained using a high tolerance is taken as an initial estimate of the solution. The final solution is obtained by a Newton–Raphson-based iterative solver with a tight tolerance. The plot of inverse mapped domain is shown in Fig. 3(c).

An important aspect of the NCM algorithm is fast and accurate evaluation of Schwarz–Christoffel integral of Eq. (23), since it is evaluated in every step of NCM for parameter evaluation,

forward map and inverse map. The basic form of the integral is

$$\int_{-1}^{+1} f(x)(1-x)^\alpha(1+x)^\beta, \quad -1 < \alpha, \beta < 1. \quad (32)$$

Endpoint singularities arise with this equation for negative values of the exponents  $(\alpha, \beta)$ . The Gauss–Jacobi quadrature formula is proposed in [13] as a modification to the Gauss quadrature method for numerical integration of kernels with singularities. However, the accuracy of integration decreases drastically if another singularity is present in the vicinity of integration interval. For maintaining high accuracy without giving up efficiency, a modified compound Gauss–Jacobi quadrature is used in this paper. In this method no singularity  $z_k$  can lie closer to an interval of integration, than half the length of that interval. For endpoints that have nearby singularities, the interval will be subdivided until the above constraint is satisfied. On a short subinterval adjacent to an endpoint, the Gauss–Jacobi quadrature is applied. On longer intervals away from the endpoint, pure Gaussian quadrature is used for integration.

### 3.3. Implementation of the NCM in NCM–VCFEM

The NCM described above, is used to construct the radial function  $\hat{f}(x, y)$  to be incorporated in the reciprocal stress function (19) for arbitrary polygonal heterogeneities. The inverse mapping function  $1/|g(w)|$  possesses the properties required of the radial function  $\hat{f}(x, y)$ , stated in conditions (20). Some of the algorithmic implementations are discussed below.

#### 3.3.1. Integration scheme for [H] and [G] matrices

The accuracy of VCFEM depends on the accuracy with which the [H] & [G] matrices in Eqs. (14) and (16) are evaluated by numerical integration over  $\Omega_m, \Omega_c, \partial\Omega_m$  and  $\partial\Omega_c$ . Singular integrals of known form may be evaluated by extensions of the Gauss quadrature rule for Cauchy principal value integrals and hyper-singular integrals [28]. However, the precondition of knowing the form of singularity has restricted its use in the present case. A method of generating discretization based on gradient of reciprocal function is used for the numerical integration of these equations. The domains  $\Omega_m, \Omega_c, \partial\Omega_m$  and  $\partial\Omega_c$  in each element are subdivided into an integration grid with two major considerations.

1. The layout of the underlying integration grid is constructed from the consideration of the functional forms of the integrand and its local gradients. The reciprocal functions of Eq. (19) containing  $1/\hat{f}(x, y)^{p+q+i-1}$  in the matrix domain  $\Omega_m$  necessitates a discretization scheme that can account for the high gradient of these functions near the interface  $\partial\Omega_c$ . Since  $\Omega_m$  may be of any arbitrary shape, the integration grid is generated by an NCM-based algorithm as shown in Fig. 5. Through the inverse mapping procedure  $z=g(w)$ , the matrix domain  $\Omega_m$  is mapped to the annular region with the interface  $\partial\Omega_c$  mapped onto the outer circumference of the unit circle. The mapped annular region is first discretized into a set of subregions. Radial lines are generated from points

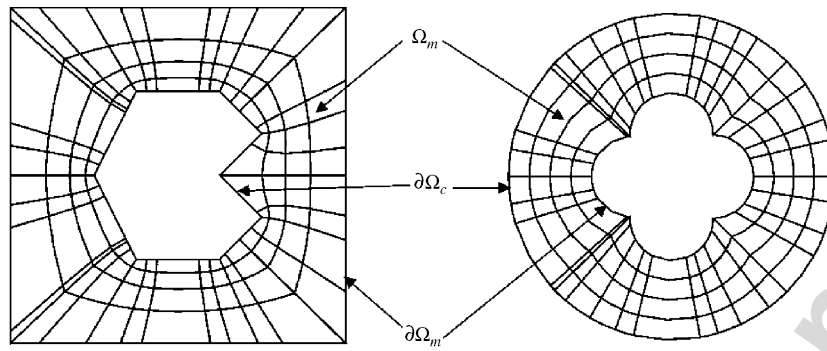


Fig. 5. Creation of subdomains for integration in the matrix domain  $\Omega_m$ .

on the circle boundary to its center and each line segment between the two boundaries is subdivided into segments of equal length. The grid in the mapped domain is then created by joining the edges of these line segments in the circumferential direction. This grid is mapped back to actual domain  $\Omega_m$  using the transformation function (23). The inherent nature of this mapping function transforms a radially uniform grid in circular domain to a graded integration grid with high grid density near the interface in  $\Omega_m$ .

2. For area integration, the number of Gauss quadrature points depends on the order of the polynomial function of the integrand and its local gradients. Optimal assignment of integration points can add to computational efficiency. The number of quadrature points for quadrilaterals in the subgrid that are far from the interface is decided by the order of the pure polynomial in stress function  $\Phi^m$ . The number of quadrature points is increased linearly, moving inwards from the element boundary to the interface.

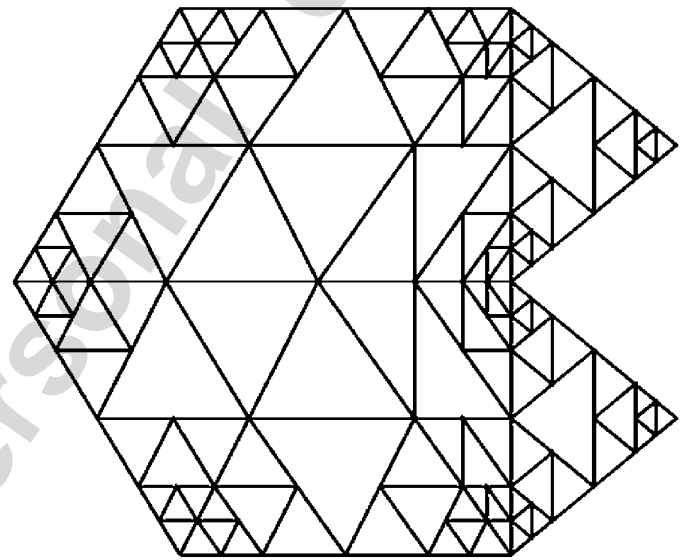


Fig. 6. Creation of subdomains for integration in the inclusion domain  $\Omega_c$ , with high density of integration points near sharp corners.

Numerical integration over the arbitrary shaped inclusions  $\Omega_c$  is conducted by applying Gauss quadrature over a triangular subgrid as shown in Fig. 6. The integration grid for a concave polygon is generated by first breaking it down to convex sub-polygons and subsequent triangularization of these convex domains about their centroid. The number of quadrature points is determined from the order of the polynomial  $\Omega_c$ .

Line integrations along  $\partial\Omega_m$  and  $\partial\Omega_c$  are evaluated by 1D Gauss quadrature along the element boundary. A special treatment is required for the integration along  $\partial\Omega_c$  due to the high gradient of stress functions near corners. Smaller segments are created near the corners using a graded subdivision. This assures higher density of integration points near the corners. The same order of Gauss quadrature is used in all the segments because computational cost for line integration is only of order  $O(n)$ , compared to order  $O(n^2)$  for area integration.

The overall computational efficiency of NCM–VCFEM depends on number of integration points. For example, the evaluation of  $[P^m]$  using inverse mapping (see flow chart 4) is done at every integration point and consequently the CPU time taken for its evaluation is significant in comparison with the total analysis time. However, this evaluation is done only once at the beginning of analysis. Therefore, even though the advantage

with efficiency may not be so obvious for elastic problems with a single time step, the efficiency will be significantly improved in non-linear problems involving multiple time steps.

### 3.3.2. Stability conditions and adaptivity in VCFEM

Stability conditions for VCFEM and adaptivity using error analysis have been discussed in [2] and the same conditions are applied in this analysis. For stability, the matrix  $[H]$  in Eq. (14) should be positive definite, for which the necessary condition is that the compliance tensor  $[S]$  be positive definite. Additional stability conditions should be satisfied to guarantee non-zero stress parameters  $\beta$  for all non-rigid body displacement fields on the element boundary or interface. This is accomplished by choice of the dimensions of the stress and displacement subspaces, i.e.  $n_\beta^m > n_q^E - 3$  and  $n_\beta^c > n_q^c - 3$ . Here  $(n_\beta^m, n_\beta^c)$  and the stress degrees of freedom in the matrix and inclusion and  $(n_q^E, n_q^c - 3)$  are the displacement degrees of freedom on the element boundary and interface, respectively.

As discussed in [2], the VCFEM formulation inherently has two sources of errors in the formulation due to weak satisfaction

of the governing equations. These are (i) the error in traction reciprocity at the element and interface boundaries and (ii) the error in strain–displacement or kinematic relations. The error in traction reciprocity is enhanced in the presence of sharp corners with traction discontinuity. As discussed in [2], displacement adaptations are implemented through boundary refinement by  $h$ -adaptivity and polynomial enrichment by  $p$ -adaptivity to reduce this error. In addition, the kinematic error can be reduced by stress function enrichment as done in [2].

**4. Multi-resolution wavelet functions for heterogeneities with sharp corners**

Sharp corners in the polygonal inclusion lead to high stress gradients in its vicinity. Simple stress field representation in terms of high order polynomial function is not adequate to capture the stress gradient. Fig. 14 shows a comparison of the stress distribution obtained by a VCFEM simulation using polynomial and NCM-based reciprocal stress fields (case 1) with that generated by an ABAQUS simulation using a very high resolution mesh with large degrees of freedom. It is evident that there is significant discrepancy between these two solutions and the NCM–VCFEM solution needs to be augmented. The use of high order polynomial interpolations in NCM–VCFEM gives rise to instabilities and leads to oscillations in the stress solution. To avert this behavior, a local stress function augmentation using multi-resolution wavelet functions is implemented. Multi-resolution wavelet stress functions have been recently incorporated into an extended VCFEM or X-VCFEM formulation in [7] to model multiple cohesive crack propagation. Wavelet bases are  $L^2(\mathcal{R})$  and generally have compact support [15,16]. Only the local coefficients in wavelet approximations are affected by sharp changes in the solution, which makes the wavelet basis a desirable tool for problems with high solution gradients. In this paper, multi-resolution wavelet functions of [7] are used to enrich both inclusion and matrix stress functions for capturing high stress gradients near the inclusion corners as

$$\Phi^m = \Phi_{\text{poly}}^m + \Phi_{\text{rec}}^m + \Phi_{\text{wvlt}}^m \quad \text{and} \quad \Phi^c = \Phi_{\text{poly}}^c + \Phi_{\text{wvlt}}^c. \quad (33)$$

Gaussian functions  $G(x) = e^{-((x-b)/a)^2/2}$ , for which the first and second derivatives  $\Psi_{a,b}^{G_1} = -1(d/dx)(e^{-((x-b)/a)^2/2})$  and  $\Psi_{a,b}^{G_2} = (d^2/dx^2)(e^{-((x-b)/a)^2/2})$ , respectively, are good candidates for wavelets bases [7,29]. These are used for stress functions and stresses in the neighborhood of each inclusion corner.

The dilation and translation parameters  $a$  and  $b$ , respectively, can be adjusted to provide high refinement and resolution at critical locations. The wavelet-based stress functions  $\Phi_{\text{wvlt}}^{m/c}$  are constructed in a local orthogonal coordinate system  $(\xi, \eta)$ , with origin at the centroid of each inclusion and parallel to global  $x, y$  coordinates. The corresponding stress function component for the Gaussian wavelet basis is

$$\Phi_{a,b,c,d}(\xi, \eta) = e^{-((\xi-b)/a)^2/2} e^{-((\eta-d)/c)^2/2} \beta_{a,b,c,d}, \quad (34)$$

where  $(a, c)$  and  $(b, d)$  are dilation and translation parameters, respectively, that can take arbitrary continuous values. For implementation in multi-resolution analysis involving discrete levels, the translation and dilation parameters should be expressed as discrete multiples of some starting values. Consequently, these discrete values  $a_m, b_n, c_k$  and  $d_l$  are expressed as

$$\begin{aligned} a_m &= a_1 \cdot (\text{tr}_a)^{m-1}, & b_n &= n \cdot b_1 \cdot a_m, \\ c_k &= c_1 \cdot (\text{tr}_c)^{k-1}, & d_l &= l \cdot d_1 \cdot c_k. \end{aligned} \quad (35)$$

Here  $(m, k)$  correspond to the levels and  $(n, l)$  correspond to the discrete translation of the bases in the  $(\xi, \eta)$  directions, respectively. The parameters  $(a_1, c_1)$  are the initial dilating values at the first level  $m = 1$ , while  $\text{tr}_a (< 1)$ ,  $\text{tr}_c (< 1)$  are the transfer rates from one level to the next higher one. The parameters  $b_1, d_1$  represent the starting values of a step translation quantity at the  $m$ th dilation level. The narrow (higher level) wavelets are translated by small steps, whereas the wider (lower level) wavelets are translated by large steps. Parameters  $\text{tr}_a = \text{tr}_c = 1$  and  $b_1 = d_1 = 0$  imply no dilation and translation, respectively. Parameters  $c_0, c_c$ , and  $d_0$  are counterparts of  $a_0, a_c$ , and  $b_0$  in the  $\eta$  direction. With the specific relations between dilation and translation parameters, the Gaussian wavelet enriched stress function in Eq. (34) becomes

$$\Phi_{m,n,k,l}(\xi, \eta) = e^{-((\xi-b_n)/a_m)^2/2} e^{-((\eta-d_l)/c_k)^2/2} \beta_{m,n,k,l}. \quad (36)$$

The family of wavelet enriched stress functions in Eq. (36) is not orthonormal, but they construct a linearly independent basis [30]. This leads to robustness and high precision in the reconstruction of any function  $f$  even with low level coefficients. The wavelet enriched stress function is thus written as

$$\Phi_{\text{wvlt}}(\xi, \eta) = \sum_{m=1, n=-n_n/2, k=1, l=0}^{m_n, n_n/2, k_n, l_n} \Phi_{m,n,k,l}(\xi, \eta). \quad (37)$$

The corresponding stresses for the wavelet enrichment alone are

$$\begin{aligned} \begin{Bmatrix} \sigma_{\xi\xi} \\ \sigma_{\eta\eta} \\ \sigma_{\xi\eta} \end{Bmatrix} &= \begin{Bmatrix} \frac{\partial^2 \Phi_{\text{wvlt}}}{\partial \eta^2} \\ \frac{\partial^2 \Phi_{\text{wvlt}}}{\partial \xi^2} \\ \frac{\partial^2 \Phi_{\text{wvlt}}}{\partial \xi \partial \eta} \end{Bmatrix} \\ &= \begin{Bmatrix} \sum_{m=1, n=-n_n/2, k=1, l=0}^{m_n, n_n/2, k_n, l_n} \frac{\partial^2 (e^{-((\xi_1-b_n)/a_m)^2/2} e^{-((\eta_1-d_l)/c_k)^2/2})}{\partial \eta^2} \beta_{m,n,k,l} \\ \sum_{m=1, n=-n_n/2, k=1, l=0}^{m_n, n_n/2, k_n, l_n} \frac{\partial^2 (e^{-((\xi_1-b_n)/a_m)^2/2} e^{-((\eta_1-d_l)/c_k)^2/2})}{\partial \xi^2} \beta_{m,n,k,l} \\ - \sum_{m=1, n=-n_n/2, k=1, l=0}^{m_n, n_n/2, k_n, l_n} \frac{\partial^2 (e^{-((\xi_1-b_n)/a_m)^2/2} e^{-((\eta_1-d_l)/c_k)^2/2})}{\partial \xi \partial \eta} \beta_{m,n,k,l} \end{Bmatrix}. \end{aligned} \quad (38)$$

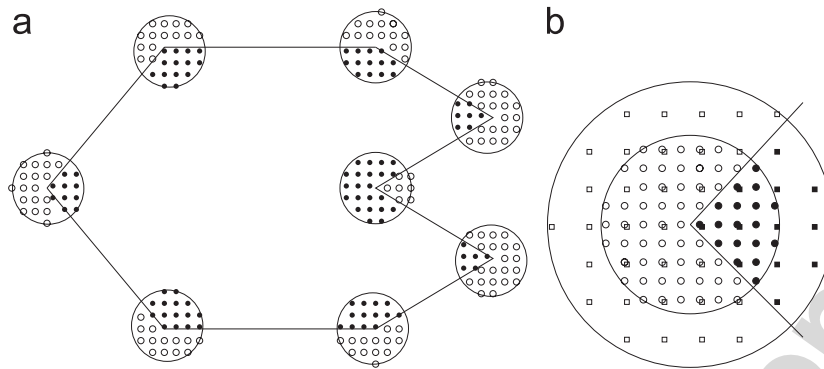


Fig. 7. (a) Regions of multi-level wavelet bases near the inclusion corners within a radius ( $R$ ); black dots correspond to wavelets inside the inclusion while the unfilled squares are for matrix domain and (b) multi-level wavelet representation: circles represent level-1 bases and squares represent level-2 bases in the matrix and inclusion.

The multi-resolution wavelet stress functions are implemented in the following steps:

1. The *level-1* domain of wavelet bases around each inclusion corner is constructed as shown in Fig. 7. Circles of a fixed radius  $R$  are drawn about each corner and each circle is overlaid with a rectangular grid of points corresponding to the position of each wavelet basis function. In Fig. 7, the points shown in black lying inside the inclusion contribute to the inclusion stress function while the remaining points (shown in white) add to the matrix stress function. Points lying at the boundary contribute to both matrix and inclusion stress functions.
2. For higher level wavelets, the same procedure is repeated with a reduced  $R = R_0(\hat{R}_c)^{m-1}$ , where  $\hat{R}_c < 1$  is a constant size reduction rate per level, and  $m$  corresponds to the level. In the higher levels, the grid is refined such that the number of wavelet base points selected in each step remains the same as shown in Fig. 7(b).
3. The integration grid for the matrix domain is able to accommodate the proper integration of wavelet functions near the corners. However, the basic triangularization-based grid in the inclusion generates a uniform set of integration points that is not adequate for integrating wavelet functions. A higher grid density is needed near the corner of  $\Omega_c$ . For each wavelet level, circles with radii proportional to dilation parameters  $a_m$  and  $c_k$  in Eq. (36) are drawn around each corner as shown in Fig. 7. The triangles inside these circles are subdivided as shown in Fig. 6 for more accurate integration.

Significant improvement in the stress gradients near the corner is observed without any spurious oscillations, by the incorporation of wavelet functions as seen in Fig. 10a.

## 5. Numerical examples for validation of NCM-VCFEM

### 5.1. A square plate with a square inclusion or hole

This example is intended to examine some convergence issues of NCM-VCFEM and also for validating its results against

those from commercial FEM codes. A square domain containing a square inclusion (composite) or void (porous) of area fraction  $A_f = 25\%$  is modeled by NCM-VCFEM. The VCFEM mesh is a single element as shown in Fig. 8a. The domain is subjected to a uniaxial stretching of  $u_x = 0.2L$  under plane strain conditions and periodic boundary condition is applied on the top surface at  $y = L$ . The properties are  $E^m = 70$  GPa,  $\nu^m = 0.33$  for the matrix material and  $E^c = 450$  GPa,  $\nu^c = 0.17$  for the inclusion material. The inclusion interface and element boundary contains 16 and 12 nodes on, respectively. The minimum number of  $\beta$  parameters are calculated from the nodal degrees of freedom according to the stability criteria mentioned in Section 3.3.2. The following range of terms are included in the construction of the stress functions:  $\Phi_{\text{poly}}^m$ :  $2 \leq p + q \leq 8$ ,  $\Phi_{\text{rec}}^m$ :  $2 \leq p + q \leq 4$ ,  $1 \leq i \leq 3$ ; for a total of 78 terms in  $\Phi^m$ , and  $\Phi_{\text{poly}}^c$ :  $2 \leq p + q \leq 8$  for a total of 42 terms in  $\Phi^c$ . For the composite, the radius of the circle of influence for the wavelet basis functions in Fig. 7 is taken as  $R = 0.1 * a$ , where  $a$  is the width of the inclusion. Higher values of  $R$  need higher number of wavelet levels  $N_{\text{level}}$ , while very small  $R$  may not adequately capture the stress concentrations in the vicinity of the corner (see also Fig. 9).

The accuracy and efficiency of the NCM-VCFEM are affected significantly by the number of wavelet levels ( $N_{\text{level}}$ ) in the multi-resolution representation. The sensitivity of the convergence of VCFEM results on the number of wavelet levels near the inclusion corner, is tested for  $N_{\text{level}} = 3$  and 4, respectively. The results are compared with those generated by an ABAQUS simulation with a model consisting of 3300 QUAD4 elements and 3361 nodes. Fig. 10 shows the stress plots along a vertical line 2, bisecting the domain. The results exhibit the convergence with respect to levels of wavelet bases for a given  $R$ . Increasing the level from 3 to 4 does not affect the results and hence the optimal level has been reached for this problem. Consequently,  $N_{\text{level}} = 3$  is chosen for  $R = 0.1 * a$  in the subsequent problems. The corresponding number of wavelet parameters are 200 for matrix in  $\Phi_{\text{wvl}}^m$  and 88 for the inclusion in  $\Phi_{\text{wvl}}^c$ .

For the composite domain with the inclusion, the stress  $\sigma_{xx}$  along the horizontal line 1 in Fig. 8a is plotted in Fig. 11a.

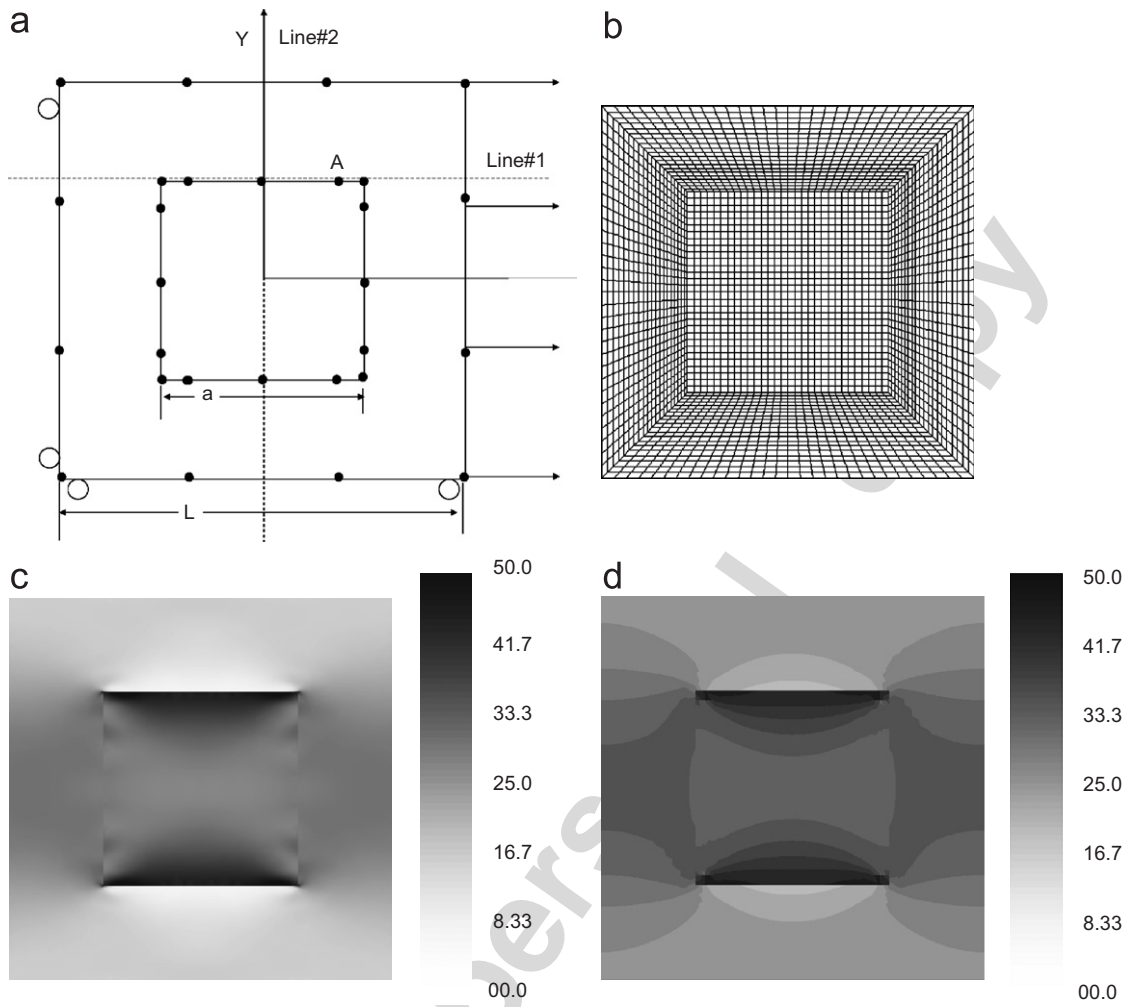


Fig. 8. (a) A single VCFEM element representing a square plate with a square inclusion of  $A_f = 25\%$  showing boundary conditions, (b) the mesh for ABAQUS analysis and stress contour plot of  $\sigma_{xx}$  by (c) VCFEM, and (d) ABAQUS.

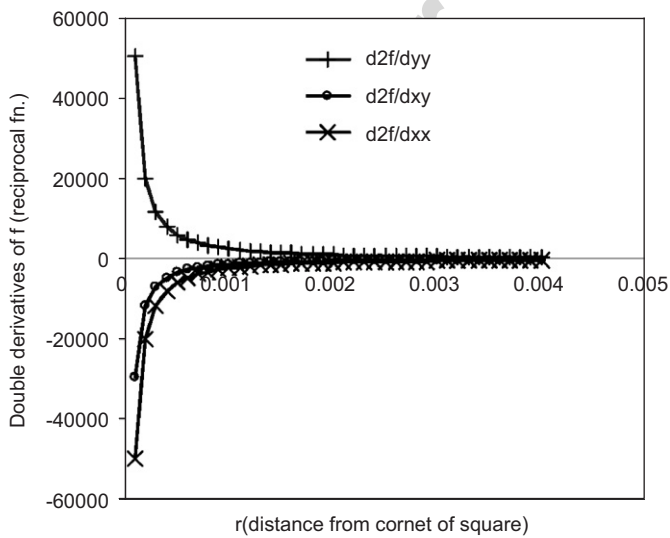


Fig. 9. Derivatives of reciprocal function ( $\partial^2 f / \partial \xi_i \partial \xi_j$ ) showing singularity at the corner point A along line #1 in Fig. 8(a).

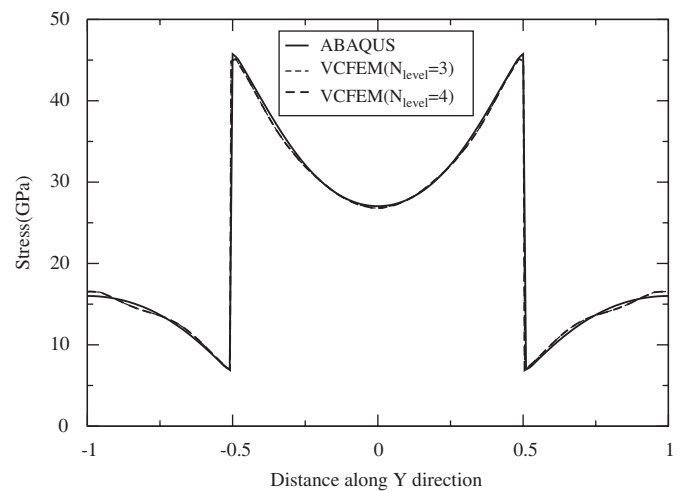


Fig. 10. Plot of  $\sigma_{xx}$  along line 2 of the square inclusion in Fig. 8(a) with different levels of wavelet bases ( $N_{level}$ ).

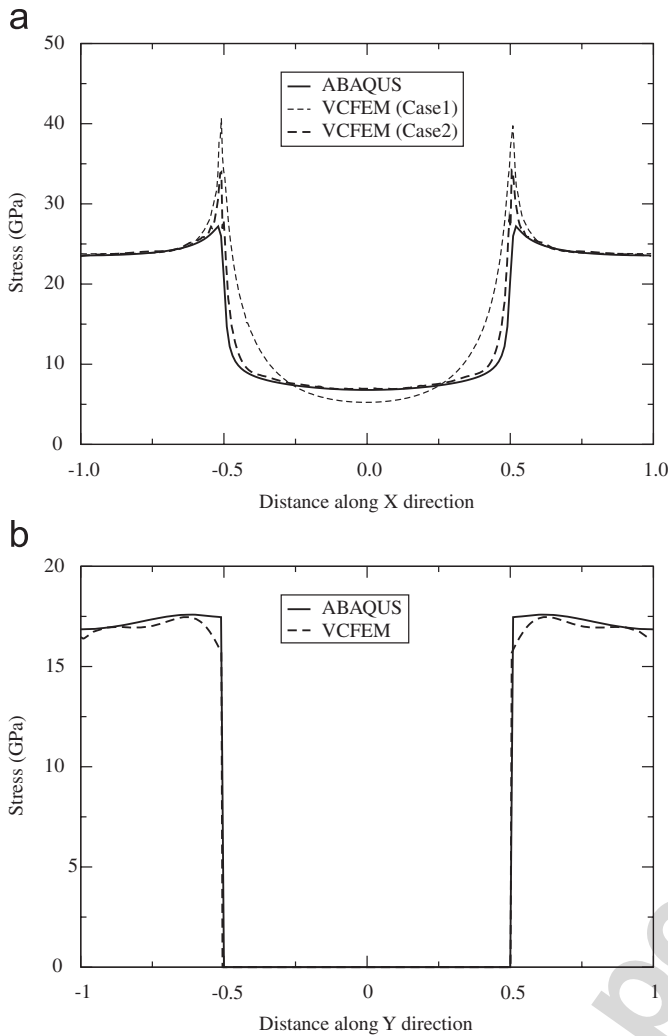


Fig. 11. (a) Plot of  $\sigma_{xx}$  along line 1 in Fig. 8(a) of square inclusion for case (1)  $\Phi^m = \Phi_{\text{poly}}^m + \Phi_{\text{rec}}^m$ ,  $\Phi^c = \Phi_{\text{poly}}^c + \Phi_{\text{wvlt}}^c$  and case (2)  $\Phi^m = \Phi_{\text{poly}}^m + \Phi_{\text{rec}}^m + \Phi_{\text{wvlt}}^m$ ,  $\Phi^c = \Phi_{\text{poly}}^c + \Phi_{\text{wvlt}}^c$  and (b) plot of  $\sigma_{xx}$  along line 2 in Fig. 8(a) of square hole ( $A_f = 25\%$ ).

This line is in the matrix just above the inclusion. The NCM–VCFEM results are compared with the refined ABAQUS model. It is evident that the stress concentration at the interface is poorly represented with this level of refinement in the ABAQUS model. The concentration is significantly better represented by the NCM–VCFEM model. The results correspond to two cases: (1) wavelet enrichment is only added to the inclusion stress function  $\Phi_{\text{wvlt}}^c$  and (2) wavelet functions are added to both the inclusion and the matrix stress functions  $\Phi_{\text{wvlt}}^m$  and  $\Phi_{\text{wvlt}}^c$ . For case (1), it is difficult to satisfy traction reciprocity at the interface since stress functions on both sides are not similar. This is manifested by a high peak with a high gradient at the interface, but a gradual decay inside of the inclusion. However, in case (2) the stress plot improves significantly with the addition of the wavelet functions to enrich the matrix phase as well. The stress gradient is much higher inside of the inclusion. The stress drops in the region adjacent to the inclusion to compensate for the increased stress inside of the inclusion.

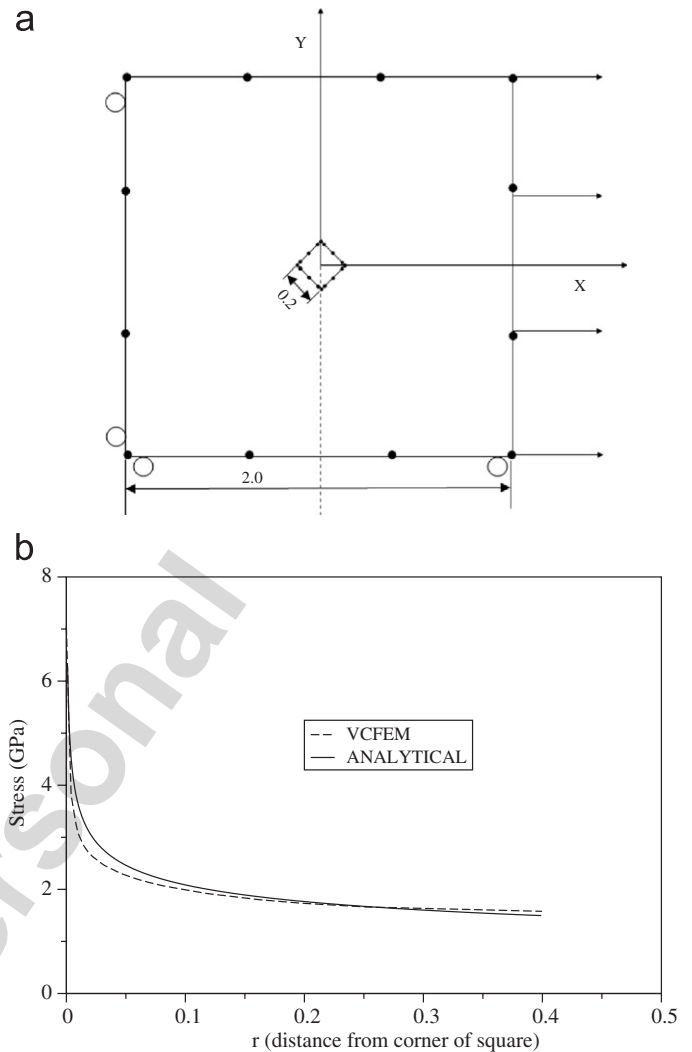


Fig. 12. Analytical result comparison with Ishikawa and Kohno [11]: (a) square plate with rigid, infinitesimal square inclusion  $A_f = 1\%$  and (b) plot of  $\sigma_{xx}$  vs.  $r$  where  $r =$  distance from point A (corner of inclusion) along  $x = 0$ .

For the case of a porous medium, when the heterogeneity is a void, the stress plot along the line 2 is shown in Fig. 11b. Again, the VCFEM results are in good agreement with ABAQUS results.

The NCM–VCFEM simulation takes 62 s on a single CPU in the Pentium 4 cluster with 2.4 GHz Intel P4 Xeon processors for the square plate with a square inclusion case, as opposed to 110 s for ABAQUS on the same machine. Without the wavelet function enrichment, the NCM–VCFEM simulation only takes 33 s. At least twice the computing efficiency is achieved with NCM–VCFEM for the simple one element example. This factor is expected to increase considerably with increasing microstructural complexity.

### 5.1.1. Comparison with analytical solution for a rigid square inclusion in an elastic infinite plate

Ishikawa and Kohno [11] have developed a semianalytical method using NCM to capture the stress singularity at the corners of a rigid square inclusion in an elastic infinite plate, as

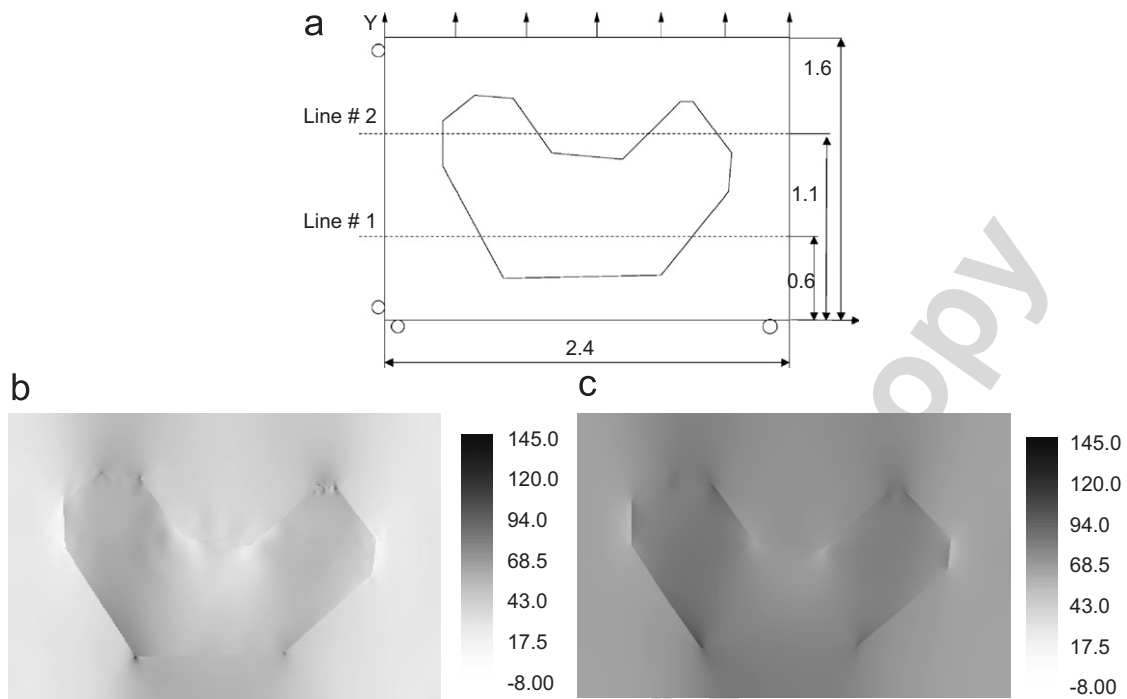


Fig. 13. (a) A square plate with an irregular concave inclusion showing the loading conditions,  $\sigma_{yy}$  stress contour plots by (b) VCFEM, and (c) ABAQUS.

shown in Fig. 12(a). The analytical expression for stress in this paper, is of the form  $K/r^\alpha$ , where  $K$  is the stress intensity factor and  $\alpha$  is a stress singularity exponent. The analytical solution is only valid in the neighborhood of the sharp corners of rigid inclusion. A similar problem is modeled with NCM-VCFEM as a check against analytical results. The inclusion area fraction in this problem is chosen to be sufficiently small ( $A_f = 1\%$ ) for infinite plate assumptions to hold. The material properties are  $E^m = 70$  GPa,  $\nu^m = 0.33$  for the matrix material and  $E^c = 450 \times 10^{10}$  GPa,  $\nu^c = 1 \times 10^{-10}$  for the inclusion material to model a nearly rigid inclusion. The boundary conditions are the same as in example of Section 5.1. The plate is subjected to uniaxial stretching  $u_x = 0.2L$  under plane strain conditions. The stress functions and displacement interpolations are also set up as in Section 5.1. The results obtained by NCM-VCFEM compares very well with the analytical solution of stress singularity near inclusion corner of Fig. 12b.

### 5.1.2. A square plate with an irregular shaped inclusion

A square plate with an irregular shaped inclusion is analyzed in this example as shown in Fig. 13a. This model is subjected to a uniaxial stretching with  $u_y = 0.33L$  under plane strain conditions. The NCM-VCFEM mesh is a single element but with an irregular concave inclusion. Periodic boundary condition is applied on the edge at  $x = L$  to manifest repeating cells. The material properties are  $E = 70$  GPa,  $\nu = 0.33$  for the matrix material and  $E = 450$  GPa,  $\nu = 0.17$  for the inclusion material. There are 12 equally spaced nodes on element boundary and 48 nodes on the matrix-inclusion boundary. As discussed in Section 3.3.1, the nodes on the interface are positioned with

increasing density near the corners to ensure accurate integration of  $[\mathbf{G}]$  matrix. This also enables better satisfaction of the traction reciprocity condition, as discussed in Section 3.3.2. The number of  $\beta$  parameters is chosen to satisfy that stability criteria. The stress functions implemented are  $\Phi_{\text{poly}}^m: 2 \leq p+q \leq 11$ ,  $\Phi_{\text{reci}}^m: 2 \leq p+q \leq 4, 1 \leq i \leq 3$ ; and  $\Phi_{\text{poly}}^c: 2 \leq p+q \leq 11$ . Wavelet functions  $N_{\text{level}} = 3$  are used. For  $R = 0.1 * a$ , the number of wavelet parameters are 164 for the matrix functions  $\Phi_{\text{wvl}}^m$  and 126 for the inclusion function  $\Phi_{\text{wvl}}^c$ . The NCM-VCFEM results obtained are compared with a very fine mesh ABAQUS model consisting of 15 842 nodes and 15 570 QUAD4 elements. The contour plots of the stress  $\sigma_{xx}$  by VCFEM and ABAQUS are shown in Figs. 13(b) and (c). Figs. 13(d) and (e) depict the stress plots along two lines passing through the inclusion of Fig. 13(a). The NCM-VCFEM results are shown for three different cases: (1) without any wavelet enrichment, (2) with wavelet enrichment in the inclusion only, and (3) wavelet enrichment in both the inclusion and matrix phases. The results clearly show the improvement of the results with wavelets and the convergence of the case (3) to the ABAQUS results. These stress gradients are very well represented with the wavelet basis enhancement. Overall, the VCFEM results are in good agreement with the ABAQUS results (see also Fig. 14).

### 5.1.3. A square plate with randomly dispersed square inclusions

A square plate with five randomly dispersed square inclusions is analyzed in this example. The NCM-VCFEM mesh, shown in Fig. 15(a), has five elements generated by Voronoi tessellation. The material properties and boundary conditions are the same

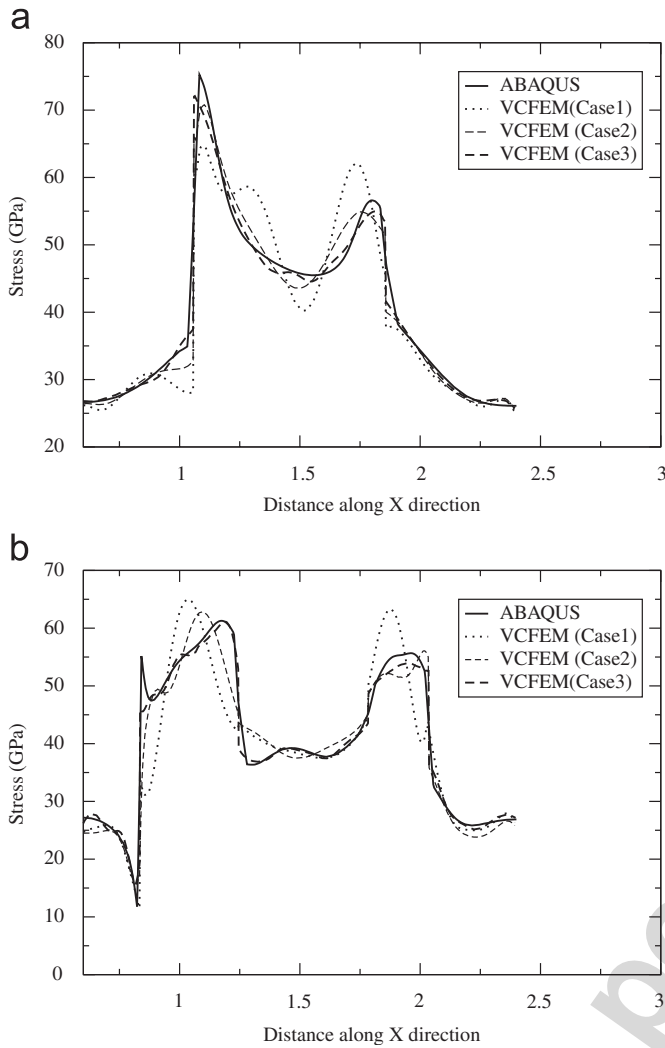


Fig. 14. Plot of  $\sigma_{yy}$  along (a) line 1 and (b) line 2 of Fig. 13; case 1 stress functions ( $\Phi^m = \Phi_{\text{poly}}^m + \Phi_{\text{rec}}^m$ ;  $\Phi^c = \Phi_{\text{poly}}^c$ ), case 2 stress functions ( $\Phi^m = \Phi_{\text{poly}}^m + \Phi_{\text{rec}}^m$ ;  $\Phi^c = \Phi_{\text{poly}}^c + \Phi_{\text{wvlt}}^c$ ), and case 3 stress functions ( $\Phi^m = \Phi_{\text{poly}}^m + \Phi_{\text{rec}}^m + \Phi_{\text{wvlt}}^m$ ;  $\Phi^c = \Phi_{\text{poly}}^c + \Phi_{\text{wvlt}}^c$ ).

as in example of Section 5.1. The plate is subjected to uniaxial stretching  $u_x = 0.02L$  under plane strain conditions. The stress functions and displacement interpolations are also set up as in Section 5.1. The contour plot of the stress  $\sigma_{xx}$  is shown in Fig. 15(b). The NCM–VCFEM stress results along a vertical line  $x = 0.25L$  is plotted and compared with the results of a fine mesh ABAQUS model (38 412 QUAD4 elements and 38 805 nodes) in Fig. 15b. Extremely good agreement is seen between the two sets of results.

#### 5.1.4. A real micrograph

In this final example, the real micrograph of Fig. 1(a) with random distribution of irregular inclusions is analyzed by NCM–VCFEM. The VCFEM mesh, generated by the modified Voronoi tessellation of Section 2, is shown in Fig. 2b. The  $\beta$  parameters are chosen based on the element with highest degree of freedom such that stability criteria [2] is also

satisfied. The stress functions are  $\Phi_{\text{poly}}^m$ :  $2 \leq p + q \leq 11$ , and  $\Phi_{\text{rec}}^m$ :  $2 \leq p + q \leq 4$ ,  $1 \leq i \leq 3$  with a total of 111 terms in  $\Phi$ . For the wavelet representation  $R = 0.1 * a$  and  $N_{\text{level}} = 3$ . The square domain is subjected to a uniaxial stretching of  $u_y = 0.004L$  under plane stress conditions. The material properties are  $E = 70$  GPa,  $\nu = 0.35$  for matrix and  $E = 165$  GPa,  $\nu = 0.27$  for inclusion. Results obtained by NCM–VCFEM are compared with a highly refined ABAQUS model with 25 928 QUAD4 elements and 26 206 nodes. From Fig. 16 it can be seen that the stress contours by both models are in good agreement.

## 6. Concluding remarks

The Voronoi cell finite element model (VCFEM) is augmented by a numerical conformal mapping (NCM)-based stress function enhancement method in this paper for capturing the effects irregular shapes of heterogeneities like particles and voids in the microstructure. Micrographs of heterogeneous materials often display very irregular shapes that have considerable effects on the evolution of stresses, strains and local damage. The NCM–VCFEM developed in this paper can go a long way in predicting these local effects in real microstructures.

The NCM-based stress function construction is expensive in comparison with conformal mapping of regular shapes like ellipses and circles. Consequently, a method that differentiates between heterogeneities that can be approximated as ellipses (within acceptable tolerances) from those that should be represented as complex polygons is first developed. Once the heterogeneity representation is finalized, the tessellation process is modified to accommodate arbitrary shapes in the resulting VCFEM mesh. Subsequently, the VCFEM formulation is locally modified for those heterogeneities that have the polygonal shapes. In the assumed stress hybrid based VCFEM formulation, stress functions for the inclusion and matrix domains are appropriately chosen to account for the shape of matrix heterogeneity. Matrix stress functions consist of polynomial and reciprocal stress functions accounting for the shape. This reciprocal stress function is generated in this work by using NCM with Schwarz–Christoffel transformations. Singularity induced due to the NCM-based stress functions has serious effect on convergence of some of the integrals in VCFEM. A special method of delineating singularity zones and applying divergence theorem to reduce the order of singularity has been implemented to handle this situation. In the vicinity of sharp corners, stress gradients are very high and affect even the far field stresses. Additional wavelet bases stress functions are used in regions of high solution gradients to capture steep stress rises in these regions.

A large number of numerical examples are conducted for validating the effectiveness of NCM–VCFEM in analyzing materials with random distributions of arbitrary shaped heterogeneities. The solutions demonstrate excellent capabilities of this method for real microstructures. Extension of NCM–VCFEM to non-linear analysis with microstructural damage by particle and matrix cracking has also been implemented and will be reported in a forthcoming paper.

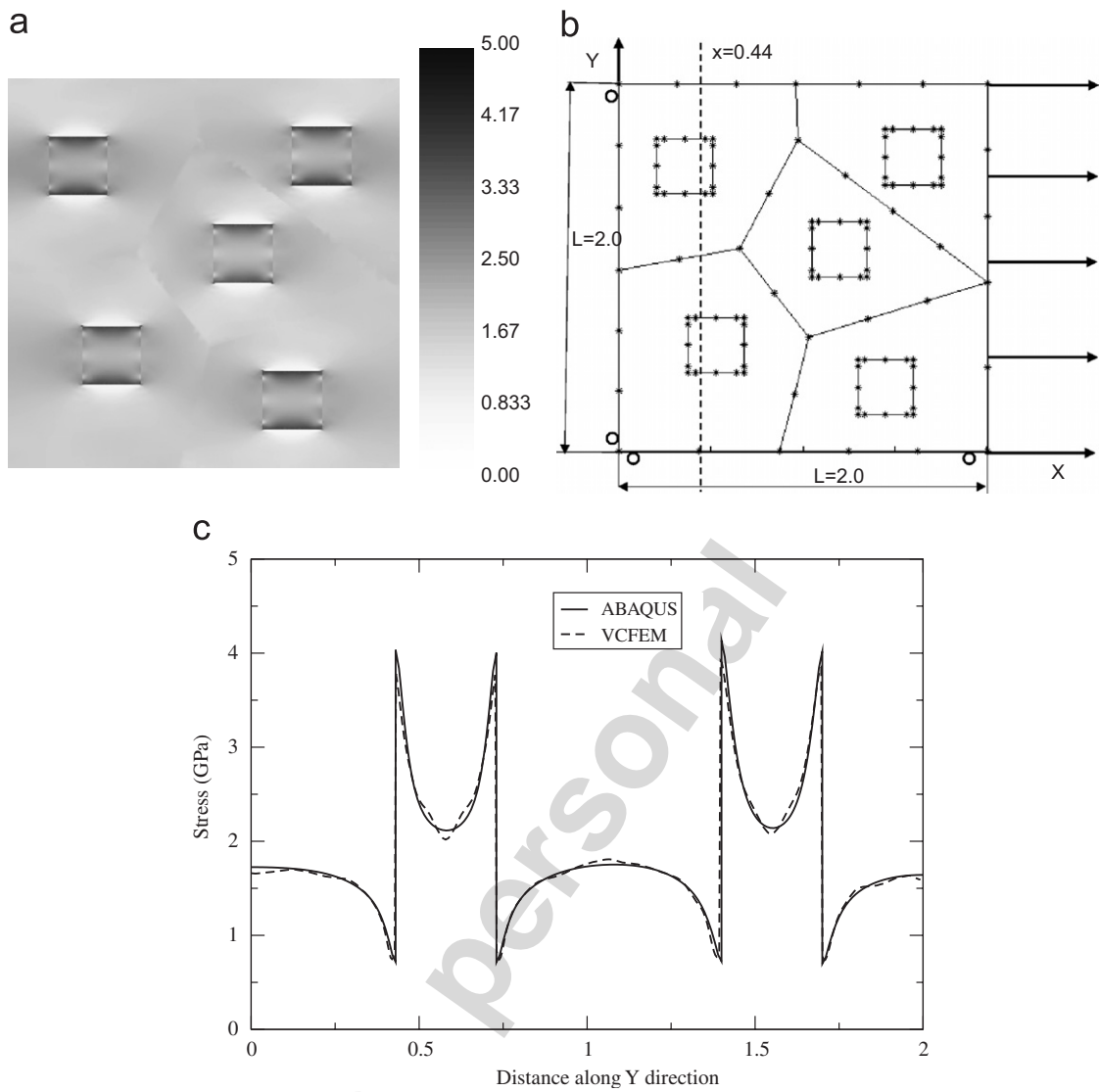


Fig. 15. Square plate with randomly distributed square inclusions (a) VCFEM mesh with loading and boundary conditions, (b) stress contour plot of  $\sigma_{xx}$  for VCFEM and (c) plot of  $\sigma_{xx}$  along line  $x = 0.44$  of Fig. 15(a).

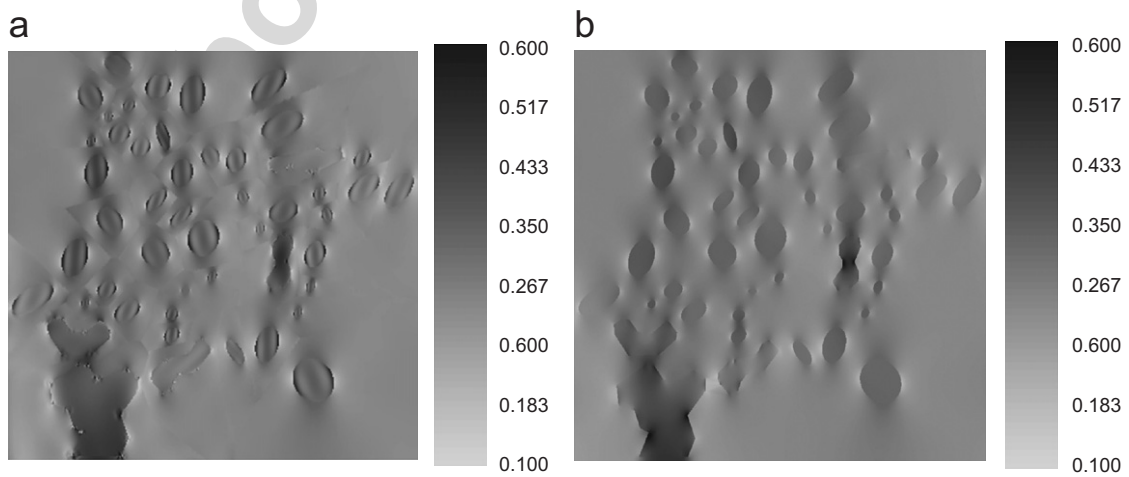


Fig. 16. Stress contour plot of  $\sigma_{yy}$  for results by (a) VCFEM and (b) ABAQUS.

Existing commercial codes have a great deal of problems in handling this class of problems.

### Acknowledgments

This work has been supported by the National Science Foundation NSF Div Civil and Mechanical Systems Division through the GOALI Grant No. CMS-0308666 (Program director: Jorn Larsen-Basse). This sponsorship is gratefully acknowledged.

### References

- [1] S. Moorthy, S. Ghosh, A model for analysis for arbitrary composite and porous microstructures with Voronoi cell finite elements, *Int. J. Numer. Methods Eng.* 39 (1996) 2363–2398.
- [2] S. Moorthy, S. Ghosh, Adaptivity and convergence in the Voronoi cell finite element model for analyzing heterogeneous materials, *Comput. Methods Appl. Mech. Eng.* 185 (2000) 37–74.
- [3] S. Ghosh, Y. Ling, M. Bhaskar, K. Ran, Interfacial debonding analysis in multiple fiber reinforced composites, *Mech. Mater.* 32 (2000) 561–591.
- [4] S. Ghosh, S. Moorthy, Particle fracture simulation in non-uniform microstructures of metal-matrix composites, *Acta Mater.* 46 (1998) 965–982.
- [5] S. Moorthy, S. Ghosh, A Voronoi cell finite element model for particle cracking in elastic–plastic composite materials, *Comput. Methods Appl. Mech. Eng.* 151 (1998) 377–400.
- [6] S. Ghosh, S. Moorthy, Three dimensional Voronoi cell finite element model for modeling microstructures with ellipsoidal heterogeneities, *Comput. Mech.* 34 (6) (2004) 510–531.
- [7] S. Li, S. Ghosh, Extended Voronoi cell finite element model for multiple cohesive crack propagation in brittle materials, *Int. J. Numer. Methods Eng.* 65 (2006) 1028–1067.
- [8] Y.L. Shen, M. Finot, A. Needleman, S. Suresh, Effective elastic response of two-phase composites, *Acta Metall. Mater.* 42 (1994) 77–97.
- [9] G.J. Rodin, Eshelby's inclusion problem for polygons and polyhedra, *J. Mech. Phys. Solids* 44 (12) (1996) 1977–1995.
- [10] M. Kawashita, H. Nozaki, Eshelby tensor of a polygonal inclusion and its special properties, *J. Elasticity* 64 (2001) 71–84.
- [11] H. Ishikawa, Y. Kohno, Analysis of stress singularities at the corner of square hole and rigid square inclusion in elastic plate by conformal mapping, *Int. J. Eng. Sci.* 31 (8) (1993) 1197–1213.
- [12] I. Tsukrov, J. Novak, Effective elastic properties of solids with defects of irregular shapes, *Int. J. Solids Struct.* 39 (2002) 1539–1555.
- [13] L.N. Trefethen, Numerical computation of the Schwarz–Christoffel transformation, *SIAM J. Sci. Stat. Comput.* 1 (1) (1980) 82–102.
- [14] T.A. Driscoll, L.N. Trefethen, Schwarz–Christoffel Mapping, Cambridge University Press, New York, 2002.
- [15] C.K. Chui, An Introduction to Wavelets, Academic Press, Boston, 1992.
- [16] R.L. Motard, B. Joseph, Wavelet Applications in Chemical Engineering, Kluwer Academic Publishers, Boston, 1994.
- [17] A. Bower, Computing dirichlet tessellations, *Comput. J.* 24 (1981) 162–166.
- [18] P.J. Green, R. Sibson, Computing dirichlet tessellations in the plane, *Comput. J.* 21 (2) (1978) 168–173.
- [19] D.M. Valiveti, S. Ghosh, Domain partitioning of multi-phase materials based on multi-scale characterizations: A Preprocessor for multi-scale modeling, *Int. J. Numer. Methods Eng.*, (in press), Published online 2006: DOI: 10.1002/nme.1834.
- [20] M. Li, S. Ghosh, O. Richmond, H. Weiland, T.N. Rouns, Three dimensional characterization and modeling of particle reinforced metal matrix composites: Part I, quantitative description of microstructural morphology, *Mater. Sci. Eng. A* 265 (1999) 153–173.
- [21] M. Li, S. Ghosh, O. Richmond, H. Weiland, T.N. Rouns, Three dimensional characterization and modeling of particle reinforced MMCs, Part II: damage characterization, *Mater. Sci. Eng. A* 266 (1999) 221–240.
- [22] M. Li, S. Ghosh, O. Richmond, An experimental–computational approach to the investigation of damage evolution in discontinuously reinforced aluminum matrix composite, *Acta Mater.* 47 (12) (1999) 3515–3532.
- [23] S. Ghosh, S.N. Mukhopadhyay, A two-dimensional automatic mesh generator for finite element analysis for random composites, *Comput. Struct.* 41 (2) (1991) 245–256.
- [24] J.C. Russ, The Image Processing Handbook, third ed., CRC Press, Boca Raton, FL, 1999.
- [25] N.I. Muskhelishvili, Some Basic Problems in the Mathematical Theory of Elasticity, P. Nordhoff Ltd., Netherland, 1965.
- [26] J. Novak, I. Tsukrov, R. Piat, E. Schnack, On contribution of pores into the effective elastic properties of carbon/carbon composites, *Int. J. Fract.* 118 (2002) 31–36.
- [27] P. Henrici, Applied and Computational Complex Analysis, Wiley, New York, 1974.
- [28] C.Y. Hui, D. Shia, Evaluations of hypersingular integrals using Gaussian quadrature, *Int. J. Numer. Methods Eng.* 44 (1999) 205–214.
- [29] J.G. Brasseur, Q. Wang, Structural evolution of intermittency and anisotropy at different scales analyzed using three dimensional wavelet transforms, *Phys. Fluids A* 4 (11) (1992) 2538–2554.
- [30] I. Daubechies, Ten Lectures in Wavelets, Society for Industrial and Applied Mathematics, Philadelphia, PA, 1992.